Green Chemistry

PAPER

View Article Online
View Journal | View Issue

Cite this: *Green Chem.*, 2026, **28**, 5240

A bio-inspired environmentally friendly and cost-effective chemo-enzymatic synthesis of (–)-ambrox from *trans*-nerolidol

Jianlin Liu,[a,b,c,d] Yi Zhang,[d] Shaoping Zhang,[a,b,c,d] Changle Zhao,[a,b,c,d] Ganlu Zhang,[e] Shengbin Zhou,[e] Xiaoguang Yan,[a,b,c,d] Weiguo Li,*[a,b,c,d] Qinggele Caiyin *[a,b,c,d] and Jianjun Qiao *[a,b,c,d]

Received 14th October 2025,
Accepted 13th November 2025

DOI: 10.1039/d5gc05456g

rsc.li/greenchem

The production of the high-value fragrance (–)-ambrox has traditionally relied on plant-derived precursors and harsh chemical processes. Inspired by the biotransformation of sclareol in fungi, we established an efficient chemo-enzymatic synthetic route of (–)-ambrox, leveraging the inexpensive starting material *trans*-nerolidol provided by *de novo* biosynthesis in *Saccharomyces cerevisiae* at a titre of 26.4 g L^{-1} in this study. To reconstruct the biosynthesis of (3*E*,7*E*)-homofarnesol, the key linear precursor for (–)-ambrox, we identified a group of naturally co-regulated enzymes comprising Baeyer–Villiger monooxygenase (BVMO), esterase and alcohol dehydrogenase through transcriptomic analysis of *H. roseonigra*. BVMO showed a broad substrate scope, with a preference towards ketones with aromatic and terpenoid substituents. Optimization of the reaction conditions and semi-rational protein engineering of subsequent squalene–hopene cyclase allowed us to obtain (–)-ambrox with 89.9% yield and 98.8% purity in a gram-level scale-up reaction. This work demonstrates an eco-friendly and cost-effective platform for (–)-ambrox biosynthesis, with potential adaptability to various terpenoids.

Green foundation

1. Compared to traditional (–)-ambrox synthesis that relies on plant-derived sclareol and toxic reagents like CrO_3 or NMU, our chemoenzymatic one-pot cascade uses renewable *trans*-nerolidol and operates under mild aqueous conditions. This biocatalytic platform demonstrates improved efficiency, safety, and sustainability, exemplifying the key green chemistry principles.
2. Our system converts inexpensive *trans*-nerolidol into (–)-ambrox in aqueous media, avoiding the use of toxic oxidants and plant extracted starting materials. The integration of cofactor regeneration also enhances atom economy and reduces waste. The gram-level scale-up reaction of the enzyme cascade under optimized reaction conditions achieves 89.9% yield and 98.8% purity *via* direct crystallization without chromatography.
3. With future improvements such as enzyme immobilization and flow chemistry integration, the platform holds strong potential for scalable and industrially viable green manufacturing.

1. Introduction

High-value terpenoids have garnered increasing attention owing to their diverse structural features and wide-ranging applications in pharmaceuticals, cosmetics, and fragrances.[1,2] (–)-Ambrox, a premium ambergris-like fragrance ingredient, contributes significantly to the global aroma chemical market, with an annual demand exceeding 100 tons.[3] Traditionally derived from the rare and ethically controversial ambergris secreted in the digestive tract of sperm whales, (–)-ambrox production has transitioned towards synthetic routes to meet ethical, regulatory, and sustainability imperatives.[4] Currently, industrial production relies primarily on semi-synthetic routes from plant-derived (–)-sclareol, a labdane-type diterpenoid extracted from *Salvia sclarea*.[5] These methods involve oxi-

[a]*School of Synthetic Biology and Biomanufacturing, Tianjin University, Tianjin 300072, China. E-mail: jianlinliu@tju.edu.cn, shaopingzhang@tju.edu.cn, 1479534625@qq.com, yanxiaoguang@tju.edu.cn, jianjunq@tju.edu.cn, qinggele@tju.edu.cn, liweiguo@tju.edu.cn*
[b]*State Key Laboratory of Synthetic Biology, Tianjin University, Tianjin 300072, China*
[c]*Key Laboratory of Systems Bioengineering (Ministry of Education), Tianjin University, Tianjin 300072, China*
[d]*Zhejiang Institute of Tianjin University (Shaoxing), Shaoxing 312300, China. E-mail: 19945620616@163.com*
[e]*School of Pharmaceutical Science and Technology, Hangzhou Institute for Advanced Study, UCAS, Hangzhou 310024, China. E-mail: zhangganlu23@mails.ucas.ac.cn, szz59@ucas.ac.cn*

dation, reduction, and cyclization to transform (−)-sclareol into (−)-ambrox through intermediates such as (+)-sclareolide and (−)-sclareol glycol.[3,6] However, such processes typically employ excessive amounts of hazardous oxidants such as chromium trioxide, osmium tetroxide, or permanganates, which pose significant environmental and safety concerns.[7,8] Additionally, the dependence on plant extraction introduces variability in raw material supply and causes volatile costs due to agricultural and climatic fluctuations.[6]

As shown in Fig. 1, to address these issues, chemo-enzymatic strategies have emerged as more sustainable alternatives.[9] One notable example is Givaudan's Ambrofix® platform, which utilizes (*E*)-β-farnesene obtained *via* fermentation as a starting material. This intermediate is chemically converted into (3*E*,7*E*)-homofarnesol and subsequently cyclized enzymatically using engineered squalene–hopene cyclase (SHC).[3] While this strategy improves atom economy and eliminates the need for plant-derived substrates, it necessitates multi-step chemical modifications, including a hazardous cyclopropanation step using *N*-methyl-*N*-nitroso-urea (NMU), a potent carcinogen and mutagen, for *in situ* diazomethane generation.[10] Despite efforts to minimize NMU usage through flow chemistry, its inclusion conflicts with green chemistry principles.[11] Furthermore, isomerization during chemical synthesis leads to the accumulation of undesired stereoisomers, compromising optical purity and sensory profiling.[12] Microbial biotransformations, including those employing *Cryptococcus albidus* ATCC 20918 and *Hyphozyma roseonigra* ATCC 20624,

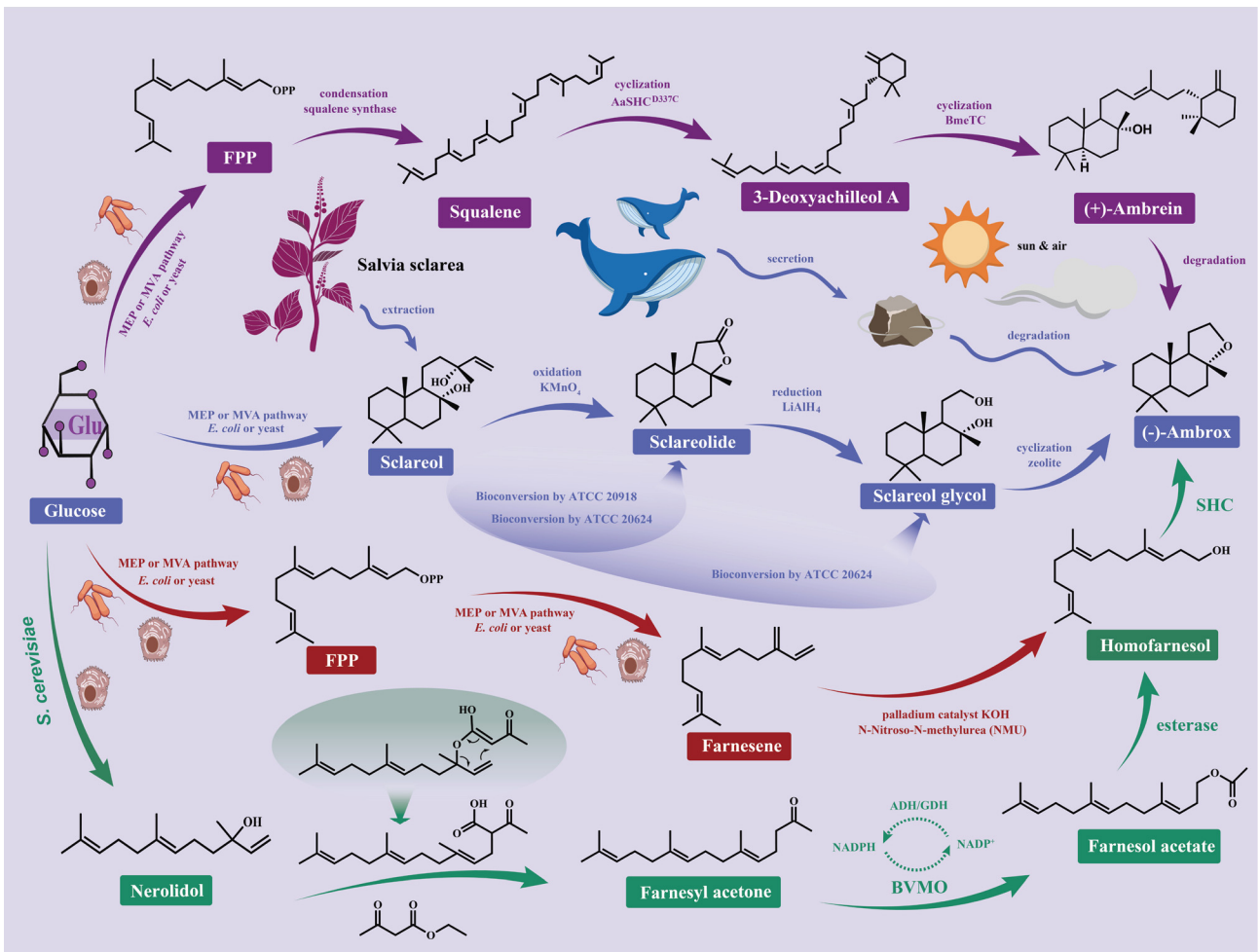

Fig. 1 Schematic overview of (−)-ambrox biosynthesis and the one-pot chemo-enzymatic cascade employed in this work. The purple arrows represent the biosynthetic pathway from squalene to (+)-ambrein and subsequently to (−)-ambrox *via* oxidative degradation. This route mimics the natural biosynthesis occurring in marine organisms and involves complex terpene cyclization steps catalyzed by triterpene cyclases. The blue arrows represent the traditional semi-synthetic route starting from (−)-sclareol extracted from *Salvia sclarea*. (−)-Sclareol is chemically oxidized to (+)-sclareolide (*e.g.*, *via* $KMnO_4$) and further reduced to (−)-sclareol glycol (*e.g.*, *via* $LiAlH_4$), followed by acid- or zeolite-catalyzed cyclization to (−)-ambrox. Although effective, this approach relies on plant-derived feedstocks and hazardous reagents. The red arrow represents Givaudan's Ambrofix® platform, which utilizes chemical transformation of homofarnesol intermediates, including palladium catalysis and mutagenic reagents such as *N*-nitroso-*N*-methylurea (NMU). The green arrow represents the eco-friendly and cost-effective pathway present in this study. Starting from *trans*-nerolidol, the pathway proceeds *via* (5*E*,9*E*)-farnesyl acetone (prepared through a green oxidative rearrangement) and catalysis by BVMO, esterase and SHC to form (−)-ambrox. NADPH regeneration is achieved *via* GDH or ADH *in situ*, enabling cofactor economy.

have also been investigated for (−)-ambrox precursor biosynthesis.[6] These fungi catalyse the selective oxidation of (−)-sclareol into (−)-ambrox precursors such as (+)-sclareolide or (−)-sclareol glycol. Nevertheless, the toxicity of hydrophobic substrates needed for these enzymatic reactions restricts achievable concentrations, thereby limiting process yields.[13] Moreover, the requirement for additional chemical steps to complete the transformation renders these biosynthetic routes impractical for achieving scalable synthesis of (−)-ambrox.[6]

To overcome these limitations, we developed a one-pot chemo-enzymatic cascade for the biosynthesis of (−)-ambrox from the readily available starting material *trans*-nerolidol, which was produced by fermentation at a titre of 26.4 g L^{-1} in *Saccharomyces cerevisiae*. Inspired by the sclareol biotransformation of *H. roseonigra*, we identified a naturally co-regulated tri-enzyme system comprising Baeyer–Villiger monooxygenase (BVMO), esterase, and alcohol dehydrogenase (ADH). This system allows for a seamless cascade for controlled and self-sufficient degradation of terpenoids: BVMO performs oxidative cleavage of ketone substrates to generate ester intermediates, which are subsequently hydrolysed by esterase to afford alcohols with a modified carbon backbone. We postulated that ADH could facilitate NADPH regeneration by consuming low-cost electron donors such as isopropanol, thus closing the cycle for cofactor regeneration. The endogenous ADH failed to be functionally expressed in *E. coli*, whereas the commercially available glucose dehydrogenase (GDH) effectively regenerated NADPH. Through systematic optimization of the reaction conditions, cofactor recycling, and enzyme quantity, we established a robust *in vitro* multi-enzymic cascade, enabling efficient conversion of (5*E*,9*E*)-farnesyl acetone to (3*E*,7*E*)-homofarnesol without intermediate isolation. Additionally, a semi-rationally evolved SHC variant was engineered to improve the final cyclization step, yielding a 3.07-fold increase in (−)-ambrox formation relative to that of the wild-type enzyme. Molecular dynamics simulations and tunnel analysis revealed that synergistic mutations (W169G and G600M) in SHC variants significantly expanded the substrate tunnel and modulated gating dynamics. Notably, we controlled the stereochemical outcome of the final ambrox product by the geometric configuration of (5*E*,9*E*)-farnesyl acetone, which can be easily synthesized from the inexpensive sesquiterpene *trans*-nerolidol. When an all-*trans* isomer is used, the resulting ambrox is exclusively (−)-ambrox. Conversely, synthesis starting from a *cis–trans* isomeric mixture yields a corresponding mixture of ambrox stereoisomers (Fig. 2). This integrated biocatalytic platform produced 0.81 g of (−)-ambrox with 98.82% purity when 1 g of (5*E*,9*E*)-farnesyl acetone was used, demonstrating excellent scalability. Notably, owing to the good yield and specificity of the designed system, (−)-ambrox isolation was achieved *via* a simple recrystallization process without chromatography, underscoring the practicality of the approach. The entire process avoids the use of any plant-extracted materials or toxic chemical reagents, eliminates concerns over isomeric impurities, and delivers optically pure (−)-ambrox under mild, environmentally friendly conditions.

Overall, by leveraging a naturally co-regulated multi-enzyme cascade and engineering key biocatalysts for enhanced performance, this platform exemplifies the principles of green chemistry—particularly in terms of waste minimization, safety, and energy efficiency—and offers a compelling solution for the industrial production of high-value fragrance compounds.

2. Methods

2.1. Strains, media and reagents

The *Escherichia coli* strain DH5α was used for plasmid construction and amplification. *E. coli* BL21 (DE3) was used for protein expression. Luria–Bertani (LB) medium (10 g L^{-1} NaCl, 10 g L^{-1}, tryptone and 5 g L^{-1} yeast extract) with ampicillin (50 μg mL^{-1}) or kanamycin (50 μg mL^{-1}) if needed was used to culture *E. coli* for plasmid extraction and protein expression. Yeast-malt medium (3 g L^{-1} yeast extract, 3 g L^{-1} malt extract, 10 g L^{-1} glucose, and 5 g L^{-1} tryptone) was used to culture *H. roseonigra* for transcriptome sequencing. Yeast extract peptone dextrose (YPD) medium (20 g L^{-1} glucose, 20 g L^{-1} peptone, and 10 g L^{-1} yeast extract) and synthetic dropout (SD) medium (20 g L^{-1} glucose, 6.7 g L^{-1} yeast nitrogen base, and 2 g L^{-1} amino acid dropout mixed powder) were used for yeast cultivation and selection of recombinant strains. The feeding solution consisted of 500 g L^{-1} glucose, 4 g L^{-1} KH_2PO_4, 4 g L^{-1} K_2HPO_4, 5.12 g L^{-1} $MgSO_4$, 3.5 g L^{-1} K_2SO_4, 10 mL L^{-1} trace metal solution, and 12 mL L^{-1} vitamin solution.

2.2. Plasmid and strain construction

The key plasmids used in this study are summarized in Table S1 and were confirmed by sequencing prior to transformation. All DNA fragments integrated into the genome of *S. cerevisiae* were generated *via* overlap extension PCR (OE-PCR). Homology-directed repair templates consisted of site-specific homologous arms (500 bp upstream and downstream of each gRNA target site) and gene expression cassettes, which included the promoter, open reading frame, and terminator. To facilitate homologous recombination in yeast, adjacent DNA fragments were designed with 50 bp overlapping regions. The primers and genes used in this study are listed in Tables S2 and S3, respectively. DNA fragments or plasmids were transformed into yeast cells using the lithium acetate/PEG/ssDNA transformation protocol for gene integration. Transformants were selected on SD medium lacking uracil at 30 °C, and several colonies were picked for overnight culture. Genomic DNA was extracted, followed by PCR verification and sequencing.

2.3. Protein expression, purification and enzyme assays

E. coli BL21 (DE3) strains containing the pET28a-SUMO plasmid were activated from glycerol stocks and grown in LB medium at 37 °C to an OD600 of 0.6 and then induced by adding 0.3 mM IPTG at 20 °C for 16 hours. The cells were harvested by centrifugation at 4 °C, 6000 rpm for 30 minutes and then resuspended in PBS buffer (1 : 8 w/v, pH 7.5). The harvested cells were sonicated on ice for 10 minutes and then cen-

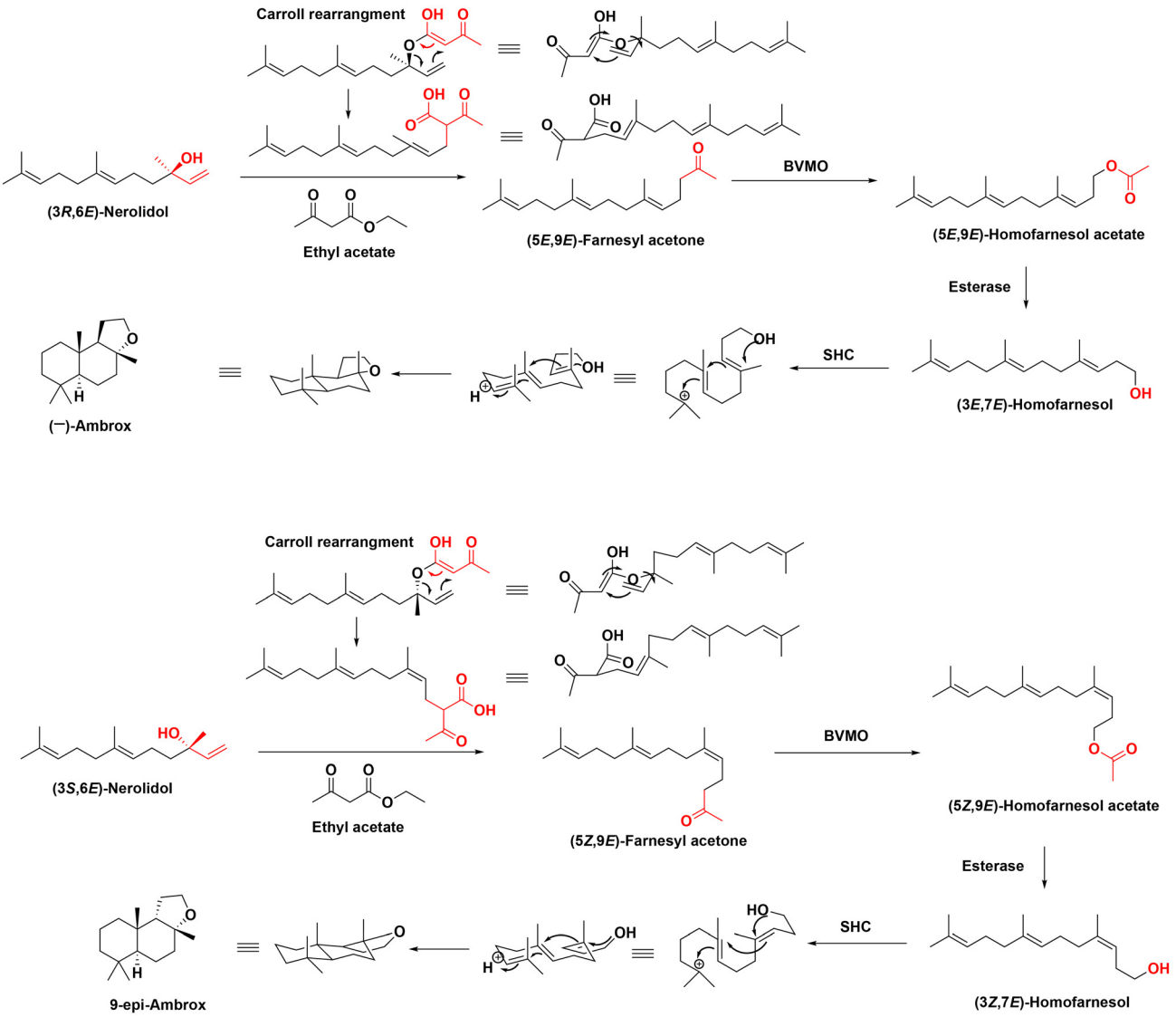

Fig. 2 Schematic illustration of the one-pot synthesis of ambrox from *trans*-nerolidol. This schematic illustrates the influence of isomers in *trans*-nerolidol on the downstream stereochemical outcome. The transformation proceeds *via* a Carroll rearrangement, where the configuration at the chiral center of nerolidol is retained and transferred to the farnesyl acetone backbone. As shown, different isomeric forms of *trans*-nerolidol yield distinct *E*/*Z*-configured farnesyl acetone moieties. This correlation underscores the critical role of starting material stereochemistry in determining the isomeric purity of the product and its downstream applications, such as in the stereoselective enzymatic synthesis of (–)-ambrox.

trifuged at 4 °C, 12 000 rpm for 15 minutes. The supernatant was transferred to a tube and kept on ice. A total of 16 μL of fragments, supernatant and pellet with 4 μL of 5× loading buffer were mixed as total protein samples, supernatant sample and precipitation sample, respectively. All samples were then boiled at 99 °C for 10 minutes to denature the proteins. After cooling, the three groups of samples were centrifuged at 12 000 rpm for 1 minute. Then, 15 μL from each group was taken for SDS-PAGE electrophoresis to assess protein expression. If further purification was required, for example, to investigate the substrate scope and kinetics of BVMO, the enzyme was purified using Ni^{2+}-affinity chromatography on an AKTA system using the N-terminal His-tags and analyzed by SDS-PAGE.

2.4. Fermentation conditions for *S. cerevisiae*

To produce *trans*-nerolidol, a two-phase fermentation strategy was employed. For shake-flask cultivation, single colonies were picked from YPD or SD plates and inoculated into 2 mL of liquid medium (YPD or SD) in 10 mL tubes. Cultures were incubated at 30 °C with shaking at 200 rpm for 20 h. Subsequently, 500 μL of the preculture was transferred into 50 mL of fresh SD-URA or YPD medium and cultivated for 96 h. After 10 h of fermentation, D-galactose was added to a final concentration of 1% (w/v), along with 5 mL of *n*-dodecane to serve as an organic overlay for extraction.

For scale-up, a 5 L bioreactor (Bailun Biotech, Shanghai) was used with 2 L of YPD medium supplemented with 2 g L^{-1}

histidine, 2 g L^{-1} leucine, trace metals, and vitamins. A frozen glycerol stock of the strain was streaked on agar to obtain fresh colonies, which were used to prepare seed cultures in 2 mL of SD medium, followed by 200 mL of YPD for two successive subcultures (18 h each, 30 °C, 220 rpm). The main fermentation was initiated with a 10% (v/v) inoculum. The pH was maintained at 5.5, the temperature was maintained at 30 °C, and dissolved oxygen was above 30%. Glucose and ethanol were used as carbon sources. Glucose feeding was adjusted to keep its concentration below 3 g L^{-1}, while ethanol was controlled under 5 g L^{-1} throughout the fermentation process.

2.5. *H. roseonigra* ATCC 20624 transcriptome sequencing

Overnight-activated *H. roseonigra* ATCC 20624 cultures were inoculated at 1% (v/v) into yeast-malt medium supplemented with varying concentrations of sclareol (0%, 0.01%, 0.05%, or 0.1% w/v). After 8 h of cultivation at 25 °C and 220 rpm, cells were harvested by centrifugation and stored at −80 °C for RNA extraction. Total RNA was isolated using the TRIzol™ reagent (Thermo Fisher Scientific, USA) according to the manufacturer's protocol. RNA integrity and concentration were assessed using an Agilent 2100 Bioanalyzer and NanoDrop spectrophotometer, respectively. Poly(A) mRNA was enriched using Oligo(dT) beads and fragmented before cDNA synthesis. Libraries were prepared *via* end repair, A-tailing, adaptor ligation, and PCR amplification, and then sequenced on an Illumina NovaSeq 6000 platform (2 × 150 bp PE). Raw reads were filtered using Cutadapt (v1.9.1) to remove adaptors and low-quality sequences. Clean reads were mapped to the *H. roseonigra* reference genome using HISAT2 (v2.2.1). Transcript abundance was calculated as FPKM using HTSeq (v0.6.1). Differential gene expression was determined using DESeq2 (v1.26.0), with $P_{adj} < 0.05$ as the significance threshold. GO and KEGG enrichment analyses were performed using GOseq and in-house scripts, respectively. Alternative splicing events were identified using rMATS (v4.1.0), and exon usage variation was assessed using DEXSeq (v1.20.1). SNVs and InDels were called with samtools and annotated using ANNOVAR. PCA and heatmaps were generated in R to evaluate data quality and sample clustering.

2.6. Chemical synthesis of sclareol acetone (compound 4)

Sclareol acetone (compound **4**) was synthesized using an adapted version of the previously reported methods.[14,15] To a stirred solution of sclareol (200 mg, 0.65 mmol, 1 equiv.) in anhydrous acetone (5 mL) were added portionwise K_2CO_3 (179.2 mg, 1.3 mmol, 2 equiv.) and $KMnO_4$ (358.9 mg, 2.27 mmol, 3.5 equiv.) under ice bath conditions. The mixture was stirred at room temperature for 2 h. After the completion of the reaction, extraction was done with a mixture of methyl *tert*-butyl ether and 5% NaOH aqueous solution (V/V = 1 : 1, 20 mL × 2), followed by extraction with methyl *tert*-butyl ether (10 mL × 2). A solution of $Na_2S_2O_3$ (10.25 mg, 6.50 mmol, 10 equiv., dissolved in water) was added to the organic phase, washed with ice water and saturated brine, and dried with anhydrous sodium sulfate; the organic phase was concentrated under ice bath conditions and freeze-dried to obtain sclareol acetone (compound **4**), a white solid (114.0 mg, yield 62.7%).

^{1}H NMR (600 MHz, $CDCl_3$) δ 2.71–2.54 (m, 2H), 2.13 (s, 3H), 1.87 (dt, J = 12.5, 3.3 Hz, 1H), 1.75 (dtd, J = 15.4, 7.9, 3.8 Hz, 1H), 1.68–1.55 (m, 3H), 1.54–1.47 (m, 1H), 1.45–1.34 (m, 4H), 1.28–1.22 (m, 2H), 1.15 (s, 3H), 1.08 (t, J = 4.4 Hz, 1H), 0.86 (s, 3H), 0.79 (d, J = 10.6 Hz, 6H). ^{13}C NMR (151 MHz, $CDCl_3$) δ 209.34, 72.73, 59.68, 55.08, 45.25, 43.49, 40.91, 39.08, 38.29, 32.40, 32.22, 28.97, 23.14, 20.50, 19.50, 17.76, 17.44, 14.18.

2.7. Optimization of the chemical synthesis of (5*E*,9*E*)-farnesyl acetone

In a 500 mL round-bottom flask equipped with a fractionating column, 22.2 g (0.1 mol) of crude *trans*-nerolidol extract and 0.2 g (0.01 mol) of aluminum isopropoxide were added. The reaction system was heated to 165 °C, and ethyl acetoacetate (14.3 g, 0.11 mol) was gradually added dropwise. The reaction temperature was maintained at 165 °C during the addition, allowing low-boiling-point byproducts to evaporate. After the completion of the addition, the system was kept at 165 °C for an additional 2 hours until CO_2 evolution ceased. The reaction was quenched by adding an equal volume of water, followed by ethyl acetate extraction. The crude product was either analyzed directly or used in subsequent reactions. The mixture was then subjected to vacuum distillation, collecting the fraction at 166–168 °C under 333 kPa, with a yield of 93%.[16] The refractive index at 20 °C was 1.4813. The proportion of the R isomer in *trans*-nerolidol determines the ratio of (5*E*,9*E*)-farnesyl acetone formed (Fig. 2). ^{13}C NMR (151 MHz, $CDCl_3$) δ 208.81, 136.38, 135.03, 131.24, 124.36, 124.05, 122.53, 43.76, 39.71, 39.63, 29.92, 26.75, 26.52, 25.69, 22.46, 17.67, 15.99, 15.98. ^{1}H NMR (600 MHz, $CDCl_3$) δ 5.11–5.06 (m, 3H), 2.45 (t, J = 7.5 Hz, 2H), 2.26 (q, J = 7.4 Hz, 2H), 2.13 (s, 3H), 2.06 (p, J = 6.9 Hz, 4H), 1.97 (q, J = 7.2 Hz, 4H), 1.68 (s, 3H), 1.62 (d, J = 1.5 Hz, 3H), 1.61–1.58 (m, 6H) (Fig. S4).

2.8. Biochemical characterization and steady kinetics of BVMO

The substrate scope was evaluated in a 2 mL reaction system. PBS buffer (pH 7.5), the substrate (final concentration: 0.2 mM), NADPH (1 mM), and 1% (v/v) DMSO were added to a 2 mL microcentrifuge tube and thoroughly mixed. BVMO was then added to a final concentration of 0.05 μM, and the reaction mixture was incubated at 25 °C for 1 hour. After incubation, an equal volume of ethyl acetate was added to extract the product. Substrate conversion and product formation were analyzed by Gas Chromatography-Mass Spectrometry (GC-MS).

To determine the relevant kinetic parameters of BVMO, (5*E*,9*E*)-farnesyl acetone (50, 75, 100, 150, 200, 300, 500, 750, and 1000 μM dissolved in DMSO) and 1 mM NADPH were added in a 2 mL tube and incubated at 25 °C. The reaction was initiated with the addition of BVMO (0.05 μM) to the reaction tubes and was allowed to proceed for 1, 2, or 4 min, respectively. After the completion of the reaction, the samples (200 μL) were extracted using 200 μL of ethyl acetate. The organic phases were dried over anhydrous sodium sulfate. Subsequently, the conver-

sion rate was detected and calculated using a gas chromatography-flame ionization detector (GC-FID). Enzyme kinetic parameters (K_M and k_{cat}) were determined by measuring the initial reaction rates at varying substrate concentrations. Data were fitted to the Michaelis–Menten equation using nonlinear regression in GraphPad Prism.

2.9. SHC low throughput rational evolution, MD directed SHC high throughput semi-rational evolution

The SHC mutant was generated through combinatorial mutations based on the amino acid sequence of the wild-type SHC. These mutations introduced targeted structural and functional modifications at the amino acid and nucleotide levels, optimizing the enzyme for the chemo-enzymatic catalytic system described in this study. This enhancement facilitates industrial-scale production.

Biocatalytic reaction. 0.5 g of engineered cells were resuspended in 10 mL of citrate–citric acid buffer (50 mM, pH 6.0). The reaction mixture contained 10 g L^{-1} (3*E*,7*E*)-homofarnesol and 0.05% (w/v) SDS and was incubated at 50 °C, 200 rpm for 24 hours. During the reaction, 0.2 mL of the sample was periodically withdrawn and extracted with 0.8 mL of *n*-hexane : isopropanol (2 : 1, v/v). The product was analyzed by gas chromatography with a GC-FID.

Molecular docking was performed 20 times for the enzyme–substrate complex using AutoDock Vina, and the most representative binding poses were selected for subsequent visualization. The substrate channel was analyzed using the CAVER online tool, based on the crystal structure of the wild-type AacSHC enzyme (PDB ID: 1UMP). Molecular dynamics (MD) simulations were carried out for both the wild-type and mutant enzymes for 200 ns each, using the Amber14SB force field and TIP3P water model for the protein, and the GAFF force field for the substrate. Principal component analysis (PCA) was performed on the MD trajectories. A total of 43 residues located within 6 Å of the active site, along with the mutated residues in the channel, were selected for distance-based analysis. The dominant conformations extracted from the MD simulations were used for tunnel calculations in CAVER, with the starting point set at the catalytic center. The probe radius, clustering threshold, shell radius, and shell depth were set to 0.9 Å, 8.0, 10 Å, and 4 Å, respectively (Fig. S1 and S2).

2.10. Reaction optimization of the enzyme cascade

All reactions were carried out in a total volume of 20 mL, using 500 mg wet cell weight of the enzyme, 3 mM (5*E*,9*E*)-farnesyl acetone, 30 μM FAD, and 1 mM NADPH as the initial reaction conditions. Reactions were conducted at 25 °C and 220 rpm for 12 hours. Unless otherwise stated, subsequent experiments were performed under the optimized conditions derived from this setup. BVMO activity was assessed in three catalytic formats: whole cells, crude enzyme, and broken cells. Due to the poor aqueous solubility of (5*E*,9*E*)-farnesyl acetone, 1% DMSO was added as a basal co-solvent to evaluate the catalytic performance of the three enzyme formats. Four additives—Tween-80, isopropanol, DMSO, and cyclodextrin—were screened for their ability to enhance biotransformation efficiency.[17] The effect of enzyme concentration on catalytic activity was examined over a range of 0 to 600 mg (wet cell weight). When assessing the impact of cofactor recycling on BVMO catalytic activity under reduced enzyme loading (200 mg cell wet weight), the concentrations of the key components were as follows: FAD at 30 μM, NADPH at either 10 μM or 25 μM, GDH at 60 nM, and glucose at 10 mM. When assessing the impact of cofactor recycling on BVMO catalytic activity under high enzyme loading (400 mg cell wet weight), the concentrations of the supplemented components were as follows: the influence of FAD concentration (0–100 μM) was evaluated. With glucose supplemented (10 mM), the glucose dehydrogenase (GDH) concentration was varied from 0 to 100 nM to support NADPH regeneration. Finally, the effect of NADPH concentration (0–80 μM) on overall catalytic efficiency was assessed.

2.11. Reaction scale-up and product recrystallization of the optimized reaction mixture

The scale-up experiment was carried out under the previously optimized conditions. The first step of the cascade, involving BVMO and esterase, was conducted at 25 °C and 220 rpm for 12 hours. Then, SHC and 0.06% SDS were added directly to the same reaction mixture, and the reaction was continued at 37 °C and 220 rpm for an additional 12 hours. Upon completion of the full cascade, the reaction mixture was extracted with ethyl acetate (10% v/v of the total volume). The organic phase was dried and the resulting crude product was subjected to recrystallization. Approximately 10 mL of warm ethanol (40–50 °C) was added to the residue, and the mixture was gently stirred until fully dissolved. The solution was then allowed to cool to room temperature, followed by the slow dropwise addition of chilled distilled water (5 mL per addition, up to ~5–10 mL in total) with light stirring to induce crystallization. The resulting suspension was transferred to an ice bath and maintained at 0–4 °C for 10–30 minutes to promote (−)-ambrox separation. If crystallization occurred, the solid was collected by centrifugation at 10 000 rpm for 5 minutes.

2.12. Data analysis

All experiments were carried out in triplicate, and the data are presented as the average of three replicates with standard error. A *t*-test was performed for statistical analysis using GraphPad Prism, and the *p*-value <0.05 (**) was considered statistically significant.

3. Results

3.1. Transcriptome analysis of *H. roseonigra* ATCC 20624 reveals the biosynthetic pathway of sclareol acetone (compound 4) to sclareol glycol

H. roseonigra is a unique fungal strain that utilizes (−)-sclareol as its sole carbon source to produce (−)-sclareol glycol, which

can subsequently be converted into (−)-ambrox.[13,18] As shown in Fig. 3A, Diao *et al*. proposed a biosynthetic pathway for (−)-sclareol glycol in *H. roseonigra* on the basis of intermediates detected during (−)-sclareol bioconversion.[19] According to their hypothesis, (−)-sclareol first undergoes a hydroxyl mutase-mediated isomerization of its C-9 side chain, yielding compound **1** (Labd-13(*E*)-ene,8α,15-diol).[19] This intermediate is subsequently oxidized at the C-15 position to form an aldehyde (compound **2**), which is further oxidized into a carboxylic acid (compound **3**). Through two sequential rounds of oxidative chain shortening, compound **3** is ultimately converted into (−)-sclareol glycol, potentially *via* a ketone intermediate (compound **4**). However, the exact enzymatic pathway for the controlled oxidative degradation of (−)-sclareol remains elusive. Notably, direct cleavage of a two-carbon unit from a ketone is chemically challenging due to the high bond dissociation energy and lack of a leaving group.[20–22] To elucidate the biosynthetic pathway of sclareol glycol, we conducted transcriptomic profiling to reveal the gene expression reprogramming induced by sclareol supplementation in *H. roseonigra.*

Transcriptomic profiling revealed that (−)-sclareol treatment induced substantial and coordinated reprogramming of the fungal gene expression landscape. Principal component analysis (PCA) and hierarchical clustering clearly demonstrated separation between the treated and control samples, confirming that substrate exposure was the dominant factor driving transcriptomic variation (Fig. 3B and C). Differential expression analysis revealed 2293 and 2551 significantly regulated genes in Experiments 1 and 2, respectively, accounting for ∼30% of all expressed genes. These transcriptional shifts included broad suppression of growth-related functions—such as ribosome biogenesis and translation—and concurrent activation of genes involved in oxidation–reduction, catabolism, and transport, indicating a shift from primary metabolism to a specialized metabolic state. As shown in Fig. 3D and E, gene ontology (GO) and KEGG pathway enrichment analyses provided a functional context revealing strong overrepresentation of redox-related functions among the up-regulated genes, such as multiple monooxygenases (*e.g.*, P450s and BVMOs), alcohol dehydrogenases and aldehyde dehydrogenases.

Interestingly, as the proposed candidate enzymes for (−)-sclareol catabolism, three genes, g3312, g3315, and g1799, were highly up-regulated under the treatment conditions (Fig. 3F). g3312, encoding a flavin monooxygenase, and g3315, an alcohol dehydrogenase, were induced more than 400–1700-fold depending on the treatment, with g1799 (esterase) also showing robust induction. Clustering analysis confirmed that the three genes share highly correlated expression profiles and likely constitute a co-regulated module.[23] We envisaged that the enzymes encoded by g3312 and g1799 catalysed Baeyer–Villiger oxidation and subsequent ester hydrolysis of the key ketone intermediate compound **4** for selective cleavage of a two-carbon unit. To validate this hypothesis, compound **4** was chemically synthesized and used as a substrate for *in vitro* enzymatic assays with the enzymes encoded by g3312 and g1799. As shown in Fig. 3G–J, compound **4** was efficiently converted to sclareol glycol *via* the corresponding acetate intermediate, thus confirming the proposed pathway and completing the missing segment of the catabolic pathway of (−)-sclareol in *H. roseonigra*.

3.2. A new strategy from *trans*-nerolidol to (−)-ambrox

Inspired by the conversion of compound **4** to sclareol glycol in *H. roseonigra*, we envisioned a biocatalytic cascade for (−)-ambrox synthesis starting from (5*E*,9*E*)-farnesyl acetone that could be facilely prepared from inexpensive (3*R*,6*E*)-nerolidol *via* a Carroll rearrangement (Fig. 4A).[16,24] Specifically, the proposed pathway involved the Baeyer–Villiger oxidation of (5*E*,9*E*)-farnesyl acetone to generate the corresponding acetate ester, followed by enzymatic hydrolysis to afford (3*E*,7*E*)-homofarnesol, which could be stereospecifically cyclized to (−)-ambrox.

To identify the most effective catalytic combination, we selected three BVMOs (g3312 mentioned above was renamed BVMO 2) with the highest expression levels for *in vitro* characterization (Fig. 5A and B). As shown in Fig. 5C, BVMO 2 exhibited the highest catalytic activity, followed by BVMO 3, whereas BVMO 1 had no activity towards (5*E*,9*E*)-farnesyl acetone. These results suggest that BVMO 1 may possess high substrate specificity, likely tolerating substrates structurally related to (−)-sclareol derivatives rather than the acyclic substrate (5*E*,9*E*)-farnesyl acetone.[25] In the screening of candidate esterases for the downstream hydrolysis step, esterase 1 (g1799 mentioned above was renamed esterase 1) demonstrated the highest catalytic efficiency, with esterase 2 and esterase 3 showing comparatively lower activities (Fig. 5D).

3.3. Exploration of the substrate scope and kinetics of BVMO

To explore its application potential in the field of biocatalysis, we evaluated the substrate range of BVMO 2 (Fig. 6A). The enzyme demonstrated broad substrate tolerance while maintaining notable selectivity.[25] Aromatic ketones were particularly well accepted, with 4-methoxyphenylacetone and 4-bromophenylacetone showing near-quantitative conversion (96% ± 3% and 96% ± 2%, respectively), indicating excellent accommodation of aromatic substituents. The enzyme also effectively catalysed the oxidation of unsaturated terpenoid ketones, including 6-methyl-5-hepten-2-one (42% ± 5%), geranyl acetone (95% ± 1%), farnesyl acetone (78% ± 2%), teprenone (57% ± 2%), and the linear aliphatic ketone 2-nonanone (87% ± 1%). The conversion rates decreased for both short-chain (6-methyl-5-hepten-2-one) and long-chain (teprenone) ketones, suggesting that spatial constraints in the active site significantly impact the catalytic performance. The observed preference for medium-chain substrates likely reflected optimal shape complementarity and favourable hydrophobic interactions within the enzyme's conformationally adaptable active site. In contrast, no activity was detected for the cyclic ketones cyclopentanone and cyclohexanone, indicating poor recognition of sterically constrained ring systems (Fig. 6B).

Enzymes involved in secondary metabolism or those that act on nonnatural substrates often exhibit lower catalytic

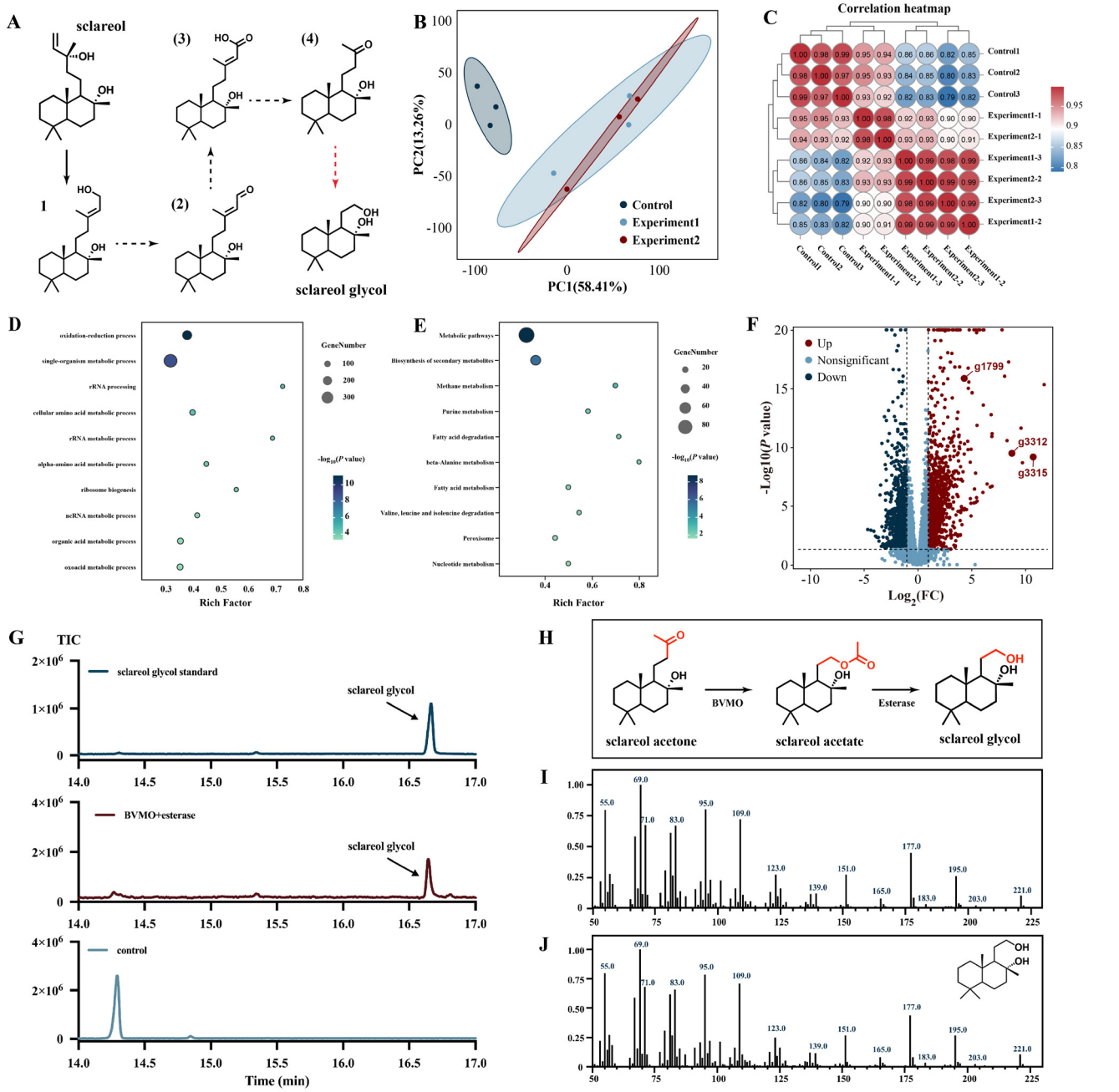

Fig. 3 Transcriptome analysis of *H. roseonigra* reveals the biosynthetic pathway of sclareol glycol. (A) Proposed biosynthetic pathway of (−)-sclareol glycol in *H. roseoniger*.[19] The solid arrows represent experimentally validated pathways, while the dashed arrows indicate proposed routes. Compound **1** denotes an experimentally confirmed intermediate, whereas compounds shown in parentheses represent hypothesized intermediates. (B) Principal component analysis (PCA) plot. Each point represents the position of a sample based on its values along the principal components. PCA reveals distinct transcriptomic shifts between the control and experiment groups. (C) Correlation heatmap of samples. High intra-group consistency ($R > 0.99$) and clear inter-group separation validate the experimental reproducibility and treatment-dependent effects. (D) GO enrichment scatter plot of differentially expressed genes. Up-regulated DEGs were primarily enriched in biological processes related to oxidation–reduction, amino acid metabolism, and cellular response to metabolic stress. (E) KEGG enrichment scatter plot of differentially expressed genes. Up-regulated genes are enriched in pathways associated with secondary metabolite biosynthesis, fatty acid degradation, and general metabolic reprogramming. (F) Volcano plot of differentially expressed genes. The *x*-axis represents the fold change in gene expression between the sample groups, while the *y*-axis indicates the statistical significance of these expression changes. Notably, three co-regulated target genes, *i.e.* g3312, g3315, and g1799, are highlighted due to their robust induction across both experimental conditions. (G) BVMO + esterase indicates the *in vitro* biocatalytic conversion of chemically synthesized sclareol acetone (compound **4**) to sclareol glycol using BVMO and esterase. Control refers to the reaction system lacking both BVMO and esterase. (H) Schematic diagram of the conversion of sclareol acetone (compound **4**) to sclareol glycol catalyzed by BVMO and esterase. (I) The mass spectrum of sclareol glycol obtained by *in vitro* biocatalytic conversion of chemically synthesized sclareol acetone (compound **4**). (J) The mass spectrum of the sclareol glycol standard.

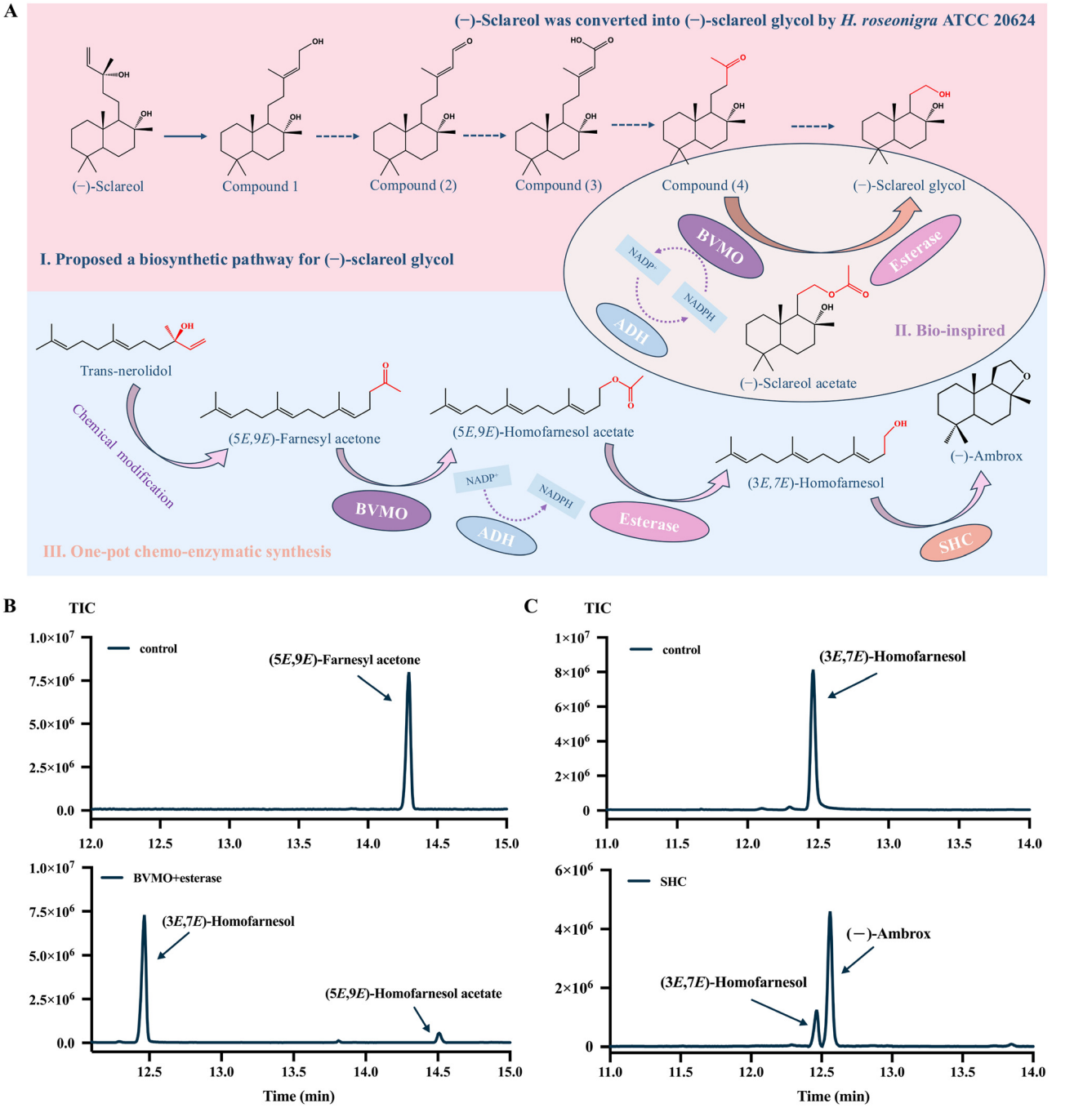

Fig. 4 Biosynthetic inspiration and transcriptome analysis of *H. roseonigra*. (A) Schematic overview of biosynthetic inspiration and the one-pot cascade strategy. Module I: proposed biosynthetic pathway of (−)-sclareol glycol in *H. roseoniger*.[19] The solid arrows represent experimentally validated pathways, while the dashed arrows indicate proposed routes. Compound **1** denotes an experimentally confirmed intermediate, whereas compounds shown in parentheses represent hypothesized intermediates. Module II: bio-inspired inference of a native BVMO-esterase system enabling selective oxidative cleavage and hydrolysis.[25,44] Module III: one-pot enzymatic cascade from *trans*-nerolidol to (−)-ambrox *via* BVMO, ADH, esterase and SHC. (B) BVMO and esterase catalyze the oxidation of (5*E*,9*E*)-farnesyl acetone to (3*E*,7*E*)-homofarnesol. BVMO + esterase indicates the *in vitro* biocatalytic conversion of (5*E*,9*E*)-farnesyl acetone using BVMO and esterase. Control refers to the reaction system lacking both BVMO and esterase. (C) SHC catalyzes the cyclization of (3*E*,7*E*)-homofarnesol to produce (−)-ambrox. SHC indicates the *in vitro* biocatalytic conversion of (3*E*,7*E*)-homofarnesol using SHC. Control refers to the reaction system lacking SHC.

efficiencies.[26] BVMO-catalysed reactions involve the nucleophilic attack of a peroxyflavin on a ketone substrate, forming a Criegee intermediate that undergoes rearrangement to generate the ester product.[27] The catalytic cycle proceeds in two half-reactions: FAD is first reduced by NADPH to generate $FADH_2$, which then reacts with molecular oxygen to form the

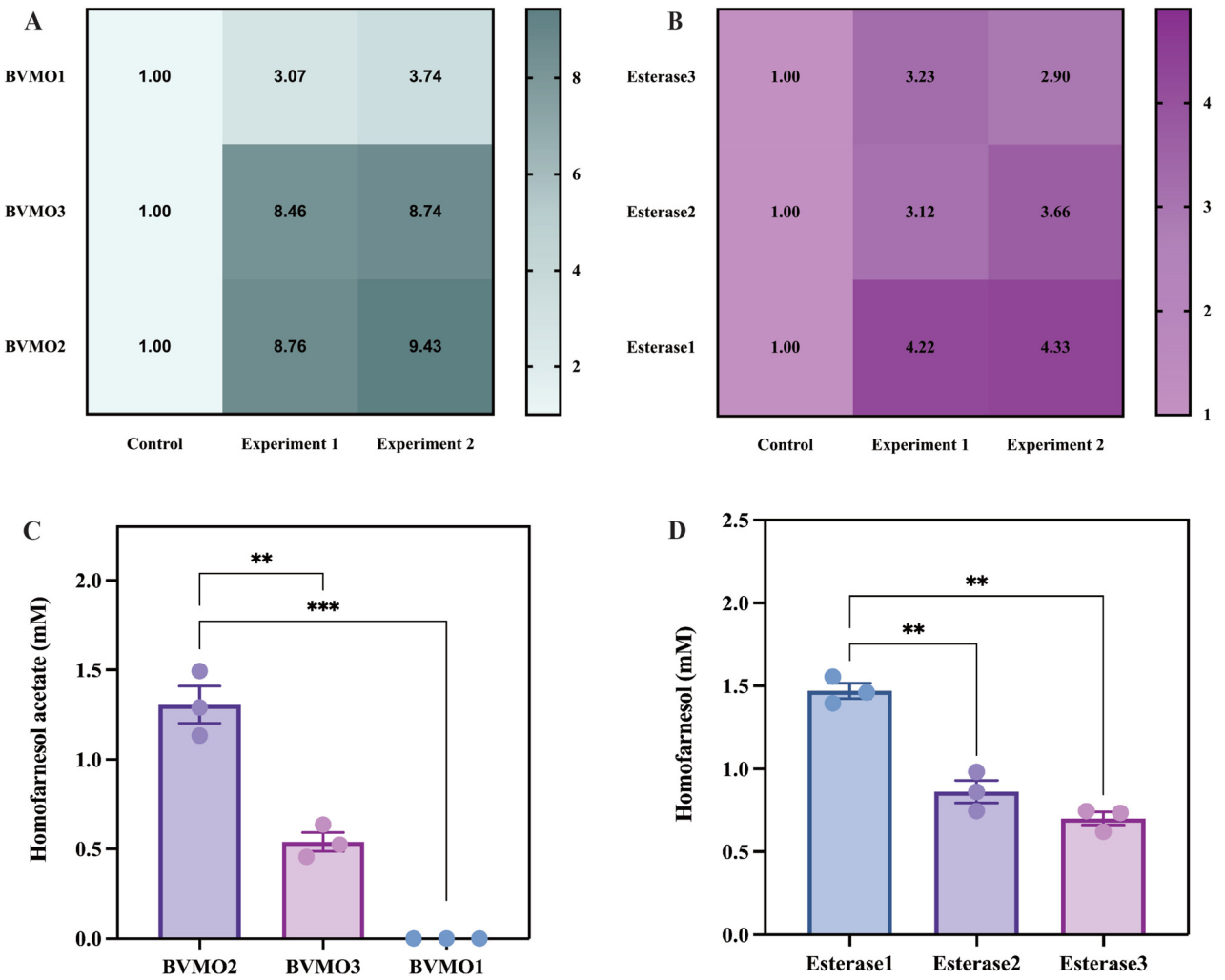

Fig. 5 Exploration of the optimal BVMOs and esterases by transcriptional analysis of *H. roseonigra* ATCC 20624. (A) Expression levels (log_2) of the three most highly expressed BVMO genes. (B) Log_2-transformed expression levels (log_2) of the three most highly expressed esterase genes. (C) Three BVMOs with the highest expression levels were used for *in vitro* characterization. Consistent with the transcriptome, BVMO 2 exhibited the highest catalytic activity, followed by BVMO 3, while BVMO 1 showed no detectable activity toward (5*E*,9*E*)-farnesyl acetone. (D) Three esterases with the highest expression levels were used for *in vitro* characterization. Consistent with the transcriptome, esterase 1 exhibited the highest catalytic activity to (5*E*,9*E*)-homofarnesol acetate, followed by esterase 2 and esterase 3.

reactive peroxyflavin.[28–30] To further assess the catalytic properties of the selected BVMO, we performed steady-state kinetic analysis using (5*E*,9*E*)-farnesyl acetone as the substrate (Fig. 6C). The enzyme exhibited a K_M of 167.7 μM and a k_{cat} of 5.06 s^{-1}, corresponding to a specific catalytic efficiency (k_{cat}/K_M) of 3.017×10^4 M^{-1} s^{-1}. These parameters fell within the characteristic range of typical enzymes, where the reported median value is approximately 10 s^{-1}, with k_{cat}/K_M values between 10^3 M^{-1} s^{-1} and 10^6 M^{-1} s^{-1}.[26]

3.4. Metabolic engineering effort for high-titre production of *trans*-nerolidol in yeast

As (5*E*,9*E*)-farnesyl acetone can be easily synthesized from the inexpensive sesquiterpene *trans*-nerolidol (Fig. 2), we aimed to improve the titre of *trans*-nerolidol in yeast to industry levels. We had previously identified a *trans*-nerolidol synthase from *Celastrus angulatus* Maxim and achieved a production titre of 7.01 g L^{-1} *trans*-nerolidol through fed-batch fermentation in a 5 L bioreactor.[31] To achieve this goal, we employed metabolic engineering strategies including linker peptides, solubility-enhancing tags, and precursor (acetyl-CoA) augmentation (Fig. 7A). We first enhanced substrate channelling between FPP and nerolidol synthase by screening linker sequences, identifying the helical linker AEAAAAKEAAAKA as optimal, resulting in a titre increase from 689.3 mg L^{-1} to 863.7 mg L^{-1} (Fig. 7B). To further increase enzyme solubility and stability, we fused a maltose-binding protein (MBP) tag to the N-terminus of nerolidol synthase, increasing the titre to 969.1 mg L^{-1} (Fig. 7C). To increase the expression of key enzymes, we next integrated the nerolidol synthase cassette into multicopy chromosomal loci (Fig. 7D). Compared with single-copy integration, the best-performing strain achieved a

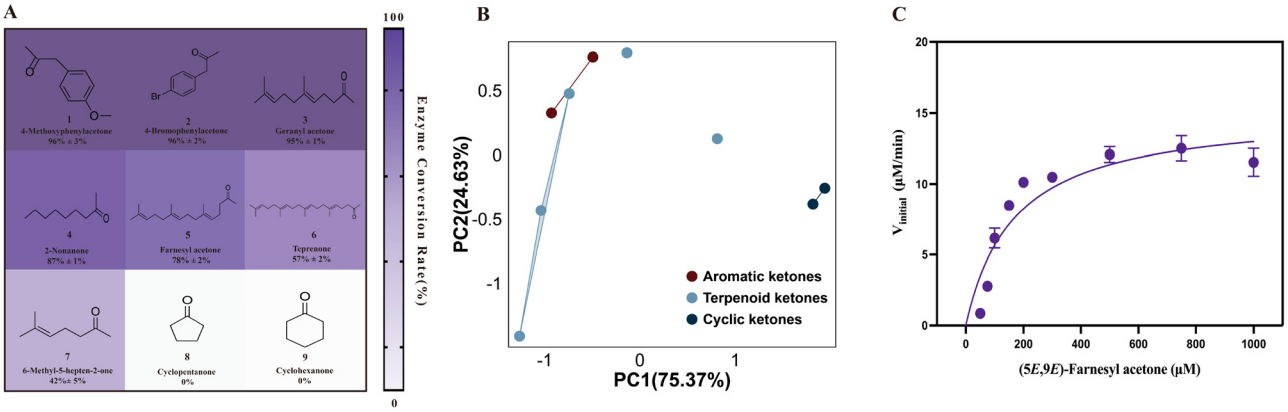

Fig. 6 The substrate scope and kinetics of BVMO. (A) Selected BVMO substrate range characterization and enzyme conversion rate detection. The conversion was determined by GC-MS after 1 hour of reaction. Conversion = [$n(\text{mol})_{\text{initial substrate}} - n(\text{mol})_{\text{residual substrate}}/n(\text{mol})_{\text{initial substrate}}$] × 100%. The heat map gradient indicates the degree of conversion, with darker colors representing higher activity. (B) Principal component analysis (PCA) plot. Each point represents the position of a sample based on its values along the principal components. PCA analysis revealed the preference of BVMO for catalyzing different types of ketones. (C) Kinetic parameters of selected BVMO on (5*E*,9*E*)-farnesyl acetone, and the data were fitted to the Michaelis–Menten equation using nonlinear regression. The plot shows the initial reaction rates of the selected BVMO 2 at varying concentrations of (5*E*,9*E*)-farnesyl acetone. The resulting curve illustrates the substrate-dependent increase in reaction velocity until approaching saturation, supporting typical saturation kinetics.

25.8% increase in nerolidol production, which reached a titre of 1212.1 mg L^{-1}. However, the modest improvement suggested a limitation in precursor availability. To address this bottleneck, we enhanced the pyruvate dehydrogenase (PDH)-bypass pathway to increase intracellular acetyl-CoA levels. This intervention significantly increased nerolidol production by 56.3%, resulting in a titre of 1894.6 mg L^{-1} under shake-flask conditions (Fig. 7E). Finally, fed-batch fermentation in a 5 L bioreactor using the optimized strain led to a *trans*-nerolidol titre of 26.4 g L^{-1} (Fig. 7F), making *trans*-nerolidol a green and sustainable feedstock for (−)-ambrox biosynthesis.

3.5. Semi-rational engineering and molecular dynamics simulation of SHC

To increase the catalytic performance of SHC in the (−)-ambrox biosynthetic cascade, we implemented a structure-guided, semi-rational engineering approach. Over 60 SHC variants—including single, double, triple, and quadruple-point mutations—were constructed and screened using (3*E*,7*E*)-homofarnesol as a substrate under uniform conditions, with the (−)-ambrox yield used as a quantitative measure of catalytic improvement (Fig. 8).[32,33] Among the single-point mutations, L80T, V375Y, and E439S presented moderate enhancements (1.17–1.59-fold), with L80T being the most effective. In contrast, mutations such as S38A, H431L, and W169G significantly reduced activity, suggesting their roles in maintaining the structural integrity or catalytic core of the enzyme (Fig. 8A). Analysis of SHC double mutants revealed limited synergistic effects, with only Q579H/F601Y (1.77-fold) and I92 V/F601Y (1.64-fold) showing clear additive or synergistic effects (Fig. 8B). Notably, triple mutants, such as W169G/L80T/G438A (2.81-fold), F129L/L80T/G438A (2.04-fold), and F129L/G438A/E439S (1.83-fold), significantly improved performance (Fig. 8C). These combinations likely enhanced multiple catalytic determinants, including hydrophobic steering, conformational flexibility, and control over carbocation migration. The most striking result emerged from the quadruple SHC mutant G600M/W169G/L80T/G438A, which achieved a 3.07-fold increase in (−)-ambrox yield relative to that of the wild-type enzyme (Fig. 8D).

The three selected SHC mutants with improved catalytic activity, W169G/L80T/G438A, W169G/F129L/G438A/E439S, and G600M/W169G/L80T/G438A, were designated M1, M2, and M3, respectively (Fig. 9). Molecular dynamics (MD) simulations coupled with CAVER analysis revealed that the engineered SHC variants (M1–M3) possessed significantly widened access tunnels compared with the wild-type enzyme (Fig. 9B–D). The most constricted tunnel "bottleneck" radius expanded from ~1.0 Å in WT to ~1.6–1.8 Å in the mutants, reflecting a more open and continuous pathway (Table 1). This structural expansion correlated strongly with the observed 2.8–3.1-fold increase in catalytic activity, suggesting that substrate diffusion through the access tunnel represents a key rate-limiting factor in the wild-type enzyme. Notably, key point mutations at the tunnel entrance and exit (W169G and G600M) act synergistically to remove steric barriers and expand the tunnel architecture. Residue G600 is located near the active site. The G600M mutation replaces the small side chain of glycine with the bulkier and more hydrophobic methionine. Among the wild-type enzymes, G600 is highly flexible and prone to collapse. The enlarged side chain of M600 serves as a structural "prop", supporting the integrity of the active site and the adjacent tunnel architecture. W169G, positioned near G600M, substitutes the large, hydrophobic tryptophan with a much smaller glycine, directly enlarging the tunnel but concurrently reducing local hydrophobicity. While W169G expands the tunnel

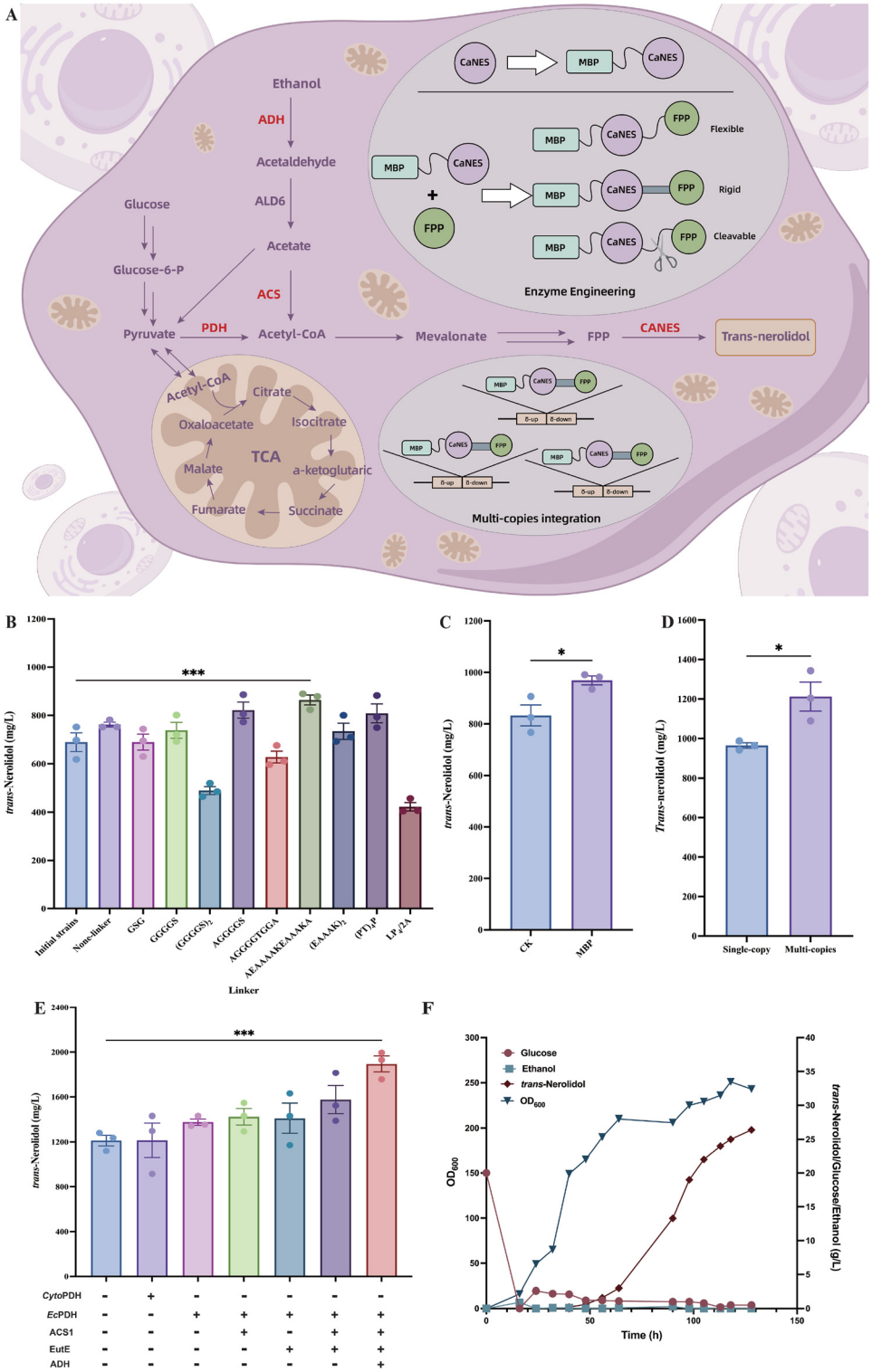

Fig. 7 Construction of a high-yield microbial cell factory for *trans*-nerolidol production. (A) Schematic overview of metabolic engineering strategies for enhancing *trans*-nerolidol production. Under enzyme engineering, solubility-enhancing tags and linker peptides were employed to boost the activity of nerolidol synthase. Under multi-copy integration, multiple genomic integration sites were used to increase the expression level of nerolidol synthase, thereby improving the overall yield. (B) Titer of *trans*-nerolidol produced using different linker peptides. (C) Effect of N-terminal solubility-enhancing tags on *trans*-nerolidol production. (D) *trans*-Nerolidol production of top-performing strains after multi-copy integration of nerolidol synthase. (E) *trans*-Nerolidol production after enhancing precursor acetyl-CoA supply *via* pyruvate dehydrogenase (PDH), alcohol dehydrogenase (ADH), aldehyde dehydrogenase (EtuE) and acetyl-CoA synthetase (ACS) introduction. (F) High-cell-density fed-batch production of *trans*-nerolidol in a 5 L bioreactor. Time-course profiles of cell growth, residual glucose, ethanol levels, and *trans*-nerolidol accumulation were recorded throughout the fermentation process to evaluate production performance.

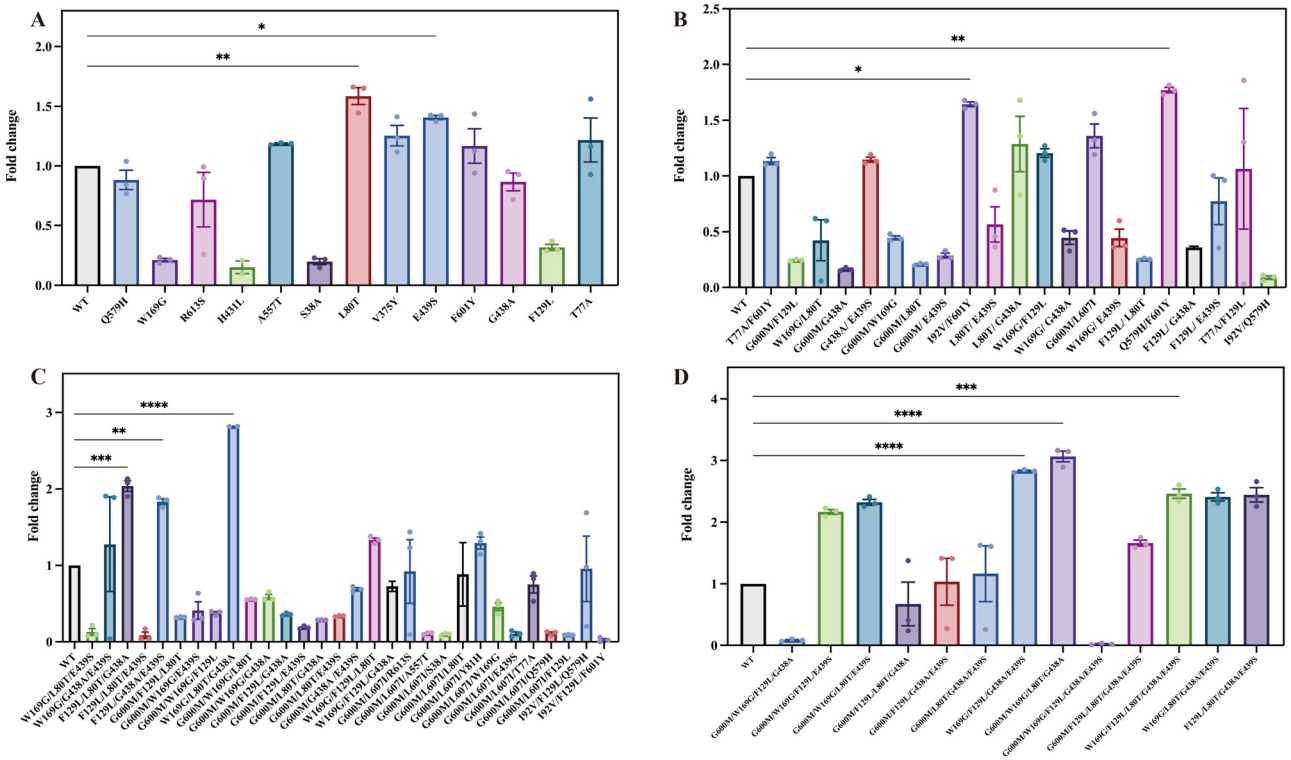

Fig. 8 Semi-rational evolution of SHC to enhance (–)-ambrox synthesis. Systematic screening of engineered SHC mutants using a low-throughput activity assay under uniform catalytic conditions. Enzyme activity was evaluated by measuring the relative (–)-ambrox yield compared to the wild-type SHC (WT), with results expressed as fold change. (A) Single-point mutant. (B) Double-point mutation. (C) Triple-point mutation. (D) Quadruple-point mutation.

dimensions, G600M compensates for the resulting loss of hydrophobicity, creating an optimized balance between steric accessibility and hydrophobic environment maintenance. This synergistic combination accounts for the most substantial structural modification, with G600M alone contributing to an ~0.7 Å increase in the bottleneck radius (M3 *vs.* M2), significantly exceeding incremental improvements from other mutations. This structure–function relationship is consistent with findings in other recent SHC engineering studies, which revealed that mutations that "loosen" constrictive active-site regions can dramatically increase turnover numbers.[32] In the M3 mutant, G600M and W169G act synergistically to eliminate steric constraints within the tunnel, resulting in an expanded channel diameter. Principal component analysis (PCA) of the MD trajectories further supported this mechanism, showing that the mutants sample a more 'open' tunnel conformation with reduced gating fluctuations relative to the wild-type (WT) enzyme.

3.6. Optimization of the biocatalytic system

To our knowledge, no previous studies have reported the integration of ADH, BVMO, esterase and SHC in one-pot cascade reactions, especially when ADH, BVMO and esterase are naturally coregulated and may form functional protein complexes. BVMOs are generally considered sluggish enzymes that require both FAD and NADPH cofactors for catalysis, making the BVMO-catalysed step typically rate limiting in multi-enzymatic cascades.[34] Therefore, we focused on optimizing the BVMO reaction conditions to improve the overall efficiency of one-pot biotransformation (Table 2).

(5*E*,9*E*)-Farnesyl acetone, poorly soluble in water, presents a significant barrier for efficient BVMO catalysis. Among the tested catalytic formats (Fig. 10A), the crude enzyme system outperformed broken and whole cells because of better substrate accessibility and product release. Whole cells exhibited minimal activity, likely due to transfer barriers across the membrane. The addition of 1% DMSO notably enhanced conversion, particularly in the crude enzyme system, by improving substrate solubility and enzyme–substrate interactions.[35] These findings underscore the importance of both the catalytic format and co-solvent selection when working with hydrophobic substrates in aqueous biocatalysis. As shown in Fig. 10B, the introduction of additives resulted in a clear increase in product yield relative to that of the additive-free control. Notably, Tween-80 yielded the greatest improvement. Systematic optimization of the reaction conditions revealed that both the reaction format and co-solvent significantly enhanced the catalytic activity of BVMO. The non-ionic surfactant Tween-80 improved the catalytic efficiency by enhancing the substrate dispersion and solubilization in aqueous media without compromising the enzyme stability. Similar findings have been reported in other terpene biotransformations, in which Tween-80 significantly promoted the conversion of hydrophobic substrates by modulating their phase distribution and increasing their bioavailability.[17] These results highlight

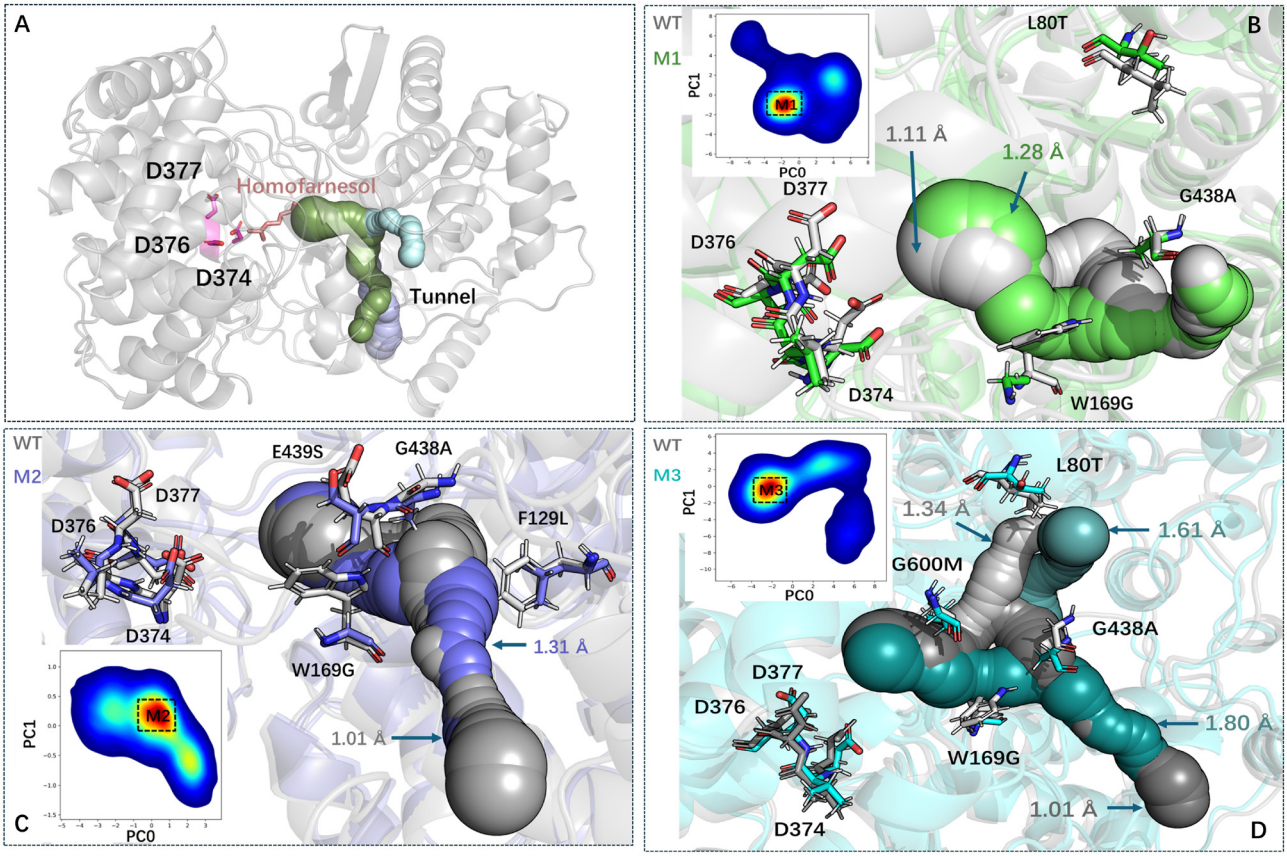

Fig. 9 Global view of the SHC substrate-access tunnel and its stepwise engineering in three generations of variants (M1–M3). (A) Overall structure of wild-type (WT) squalene–hopene cyclase (grey cartoon) complexed with the substrate (3*E*,7*E*)-homofarnesol (pink sticks). Calculated substrate tunnels are shown as coloured surfaces, and the catalytic triad D374, D376 and D377 is highlighted as magenta sticks. (B) Superposition of WT (grey) and the first-generation variant M1 (green). Key mutations W169G, L80T and G438A are indicated. These substitutions enlarge the tunnel bottleneck radius from 1.11 Å to 1.28 Å and render the tunnel surface smoother and more continuous. (C) Superposition of WT (grey) and the second-generation variant M2 (blue). Multiple mutations (W169G, F129L, G438A and E439S) collectively remodel the tunnel wall, expanding the bottleneck from 1.01 Å to 1.31 Å and further alleviating steric constraints. (D) Superposition of WT (grey) and the third-generation variant M3 (cyan). The newly introduced G600M, together with L80T, W169G and G438A, cooperatively widens several tunnel cross-sections to 1.34 Å, 1.61 Å and 1.80 Å, yielding the greatest tunnel continuity and a more stabilized exit region.

Table 1 Tunnel bottleneck radii (BR) of WT and mutant enzymes. (Average ± s.d. calculated over CAVER frames; Max = largest BR observed)

Variant	Average_BR (Å)	Max_BR (Å)
WT	1.01 ± 0.08	1.16
M1	1.18 ± 0.12	1.38
M2	1.25 ± 0.13	1.39
M3	1.71 ± 0.25	1.8

the critical role of microenvironment engineering in enabling efficient biocatalysis involving poorly water-soluble substrates.

To further optimize the BVMO-catalysed system, we systematically investigated the impact of cell loading on the conversion of (5*E*,9*E*)-farnesyl acetone. As shown in Fig. 10C, within the low-cell mass range (100–400 mg wet cell weight), product formation increased proportionally with the dosage of the catalyst, reaching a maximum at 400 mg. However, further increasing the cell mass to 500 mg and 600 mg resulted in a decrease in the product concentration, suggesting that excessive cell loading negatively affected the overall catalytic efficiency. This nonlinear decline is likely the result of multiple compounding factors. While moderate increases in cell density increase the availability of intracellular enzymes, thereby improving volumetric productivity, excessive biomass can increase system viscosity, hinder substrate dispersion, and limit product release.[36] Additionally, high cell densities may limit oxygen transfer—an especially critical factor for BVMO-catalysed monooxygenation reactions that rely on molecular oxygen as a co-substrate. This observation, given the requirement for both FAD and NADPH in BVMO catalysis, suggested that high biomass demands may reflect intracellular cofactor limitations rather than enzyme quantity.

To address cofactor limitations and improve process sustainability, we evaluated the impact of FAD and NADPH supplementation at a reduced wet cell weight of 200 mg, along with strategies for NADPH regeneration. To facilitate NADPH regeneration, we evaluated the use of either ADH or GDH.

Table 2 Quantitative comparison of sustainability metrics for different (−)-ambrox synthetic routes

Route	Starting feedstock	Atom economy (%)	*E*-Factor (kg kg^{-1})	Hazardous reagent involved
Squalene route	Squalene	27.5	2.61	None
Traditional chemical	(−)-Sclareol	54.1	0.74	CrO_3, $KMnO_4$, and $LiAlH_4$
Givaudan Ambrofix®	(*E*)-β-Farnesene	89.4	0.12	NMU and palladium
This work	*trans*-Nerolidol	80.2	0.25	None

Atom economy (AE) $= \dfrac{(M(P))}{\sum_i M(R_i)} \times 100\%$. *P*: (−)-ambrox ($C_{16}H_{28}O$). R_i: stoichiometric inputs. *E*-Factor $= \dfrac{\sum_k m(B_k)}{m(P)}$. Count only inevitable by-products B_k (water typically excluded).

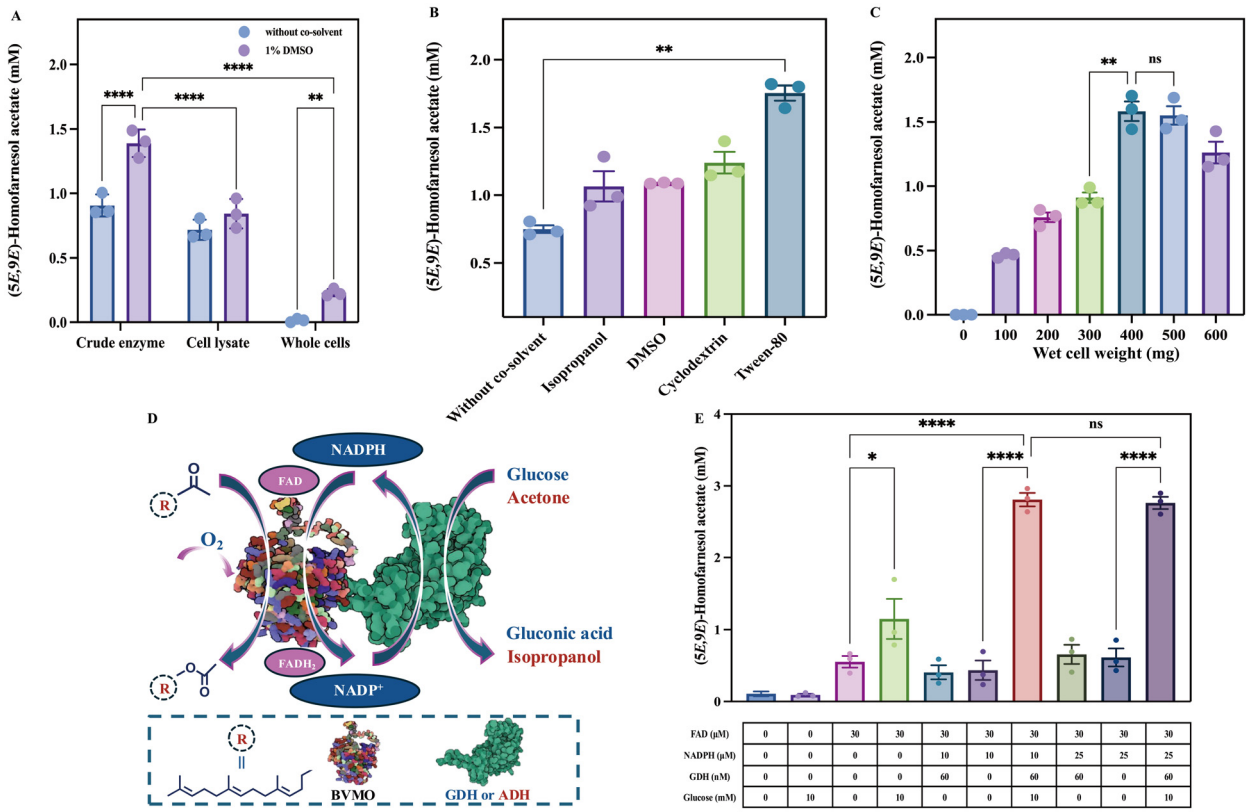

Fig. 10 Optimization of the BVMO biocatalytic reaction. (A) Effect of catalytic format on enzyme activity. "Crude enzyme" refers to the supernatant from lysed cells. "Cell lysate" refers to the whole lysate after cell disruption. "Whole cells" refer to the intact cells without lysis. "1% DMSO" refers to the addition of 1% DMSO to each catalytic format tested. (B) Effect of co-solvent type on enzyme activity. Four co-solvents—1% (v/v) DMSO, 1% (v/v) isopropanol, 0.1% (w/v) cyclodextrin, and 0.1% (v/v) Tween-80—were screened. Tween-80 showed the greatest enhancement in conversion. (C) Effect of cell density on enzyme activity. The number of cells added was expressed as wet cell weight. (D) Schematic representation of the BVMO-catalyzed oxidation of (5*E*,9*E*)-farnesyl acetone, coupled with NADPH recycling *via* GDH or ADH. The glucose or isopropanol serves as the donor for $NADP^+$ regeneration, and FAD serves as the cofactor for monooxygenase catalysis. (E) Effect of cofactor recycling on BVMO catalysis; the table indicates the amount of each component added. Impact of cofactor supplementation and regeneration on reaction efficiency. Systematic evaluation of FAD, NADPH, GDH, and glucose concentrations revealed that the full recycling system (FAD + GDH + NADPH + glucose) significantly enhanced product formation. The table below the bar graph indicates the composition of each condition tested.

Although the transcriptomic analysis of *H. roseonigra* revealed that a highly expressed ADH gene was co-regulated with BVMO and esterase candidates, heterologous expression of ADH in *E. coli* consistently resulted in insoluble inclusion bodies with no detectable activity. Despite extensive engineering efforts, including N-terminal SUMO tagging, co-expression with five different chaperone systems (DnaK–DnaJ–GrpE + GroES–GroEL, GroES–GroEL alone, DnaK–DnaJ–GrpE, GroES–GroEL–Tig, and Tig), and fusion with BVMO itself, none of these approaches yielded soluble or active ADH. As a practical alternative, we selected a commercially available GDH for NADPH recycling (Fig. 10D). As shown in Fig. 10E, either FAD or NADPH are dispensable cofactors for BVMO-mediated oxidation, as the absence of either significantly impaired product

formation. The introduction of GDH and glucose markedly enhanced the catalytic performance of BVMO, suggesting the establishment of an efficient *in situ* cofactor recycling system. Under these optimized conditions, the product concentrations reached 2.81 mM with 10 μM NADPH and 2.76 mM with 25 μM NADPH, substantially outperforming non-recycling controls (Fig. 10E). Interestingly, modest product formation was also observed when only FAD and glucose were added, indicating that endogenous GDH activity within *E. coli* could partially sustain NADPH regeneration. Moreover, the negligible difference in product yields between 10 μM and 25 μM NADPH under full recycling conditions suggests that only minimal supplementation of NADPH is needed once the regeneration system is in place (Fig. 10E), thereby reducing cofactor consumption and significantly improving the cost-effectiveness of the process.

As shown in Fig. 11, the reaction could proceed with relatively high efficiency even in the absence of exogenously added FAD or NADPH, with a high wet cell weight of 400 mg, suggesting distinct bottlenecks under high-biomass conditions. Increasing the FAD concentration to 100 μM led to only marginal improvements or even slight compromise in product yield (Fig. 11A), possibly due to disruption of protein conformational or redox balance in the system.[37] Product formation was still observed in the absence of added GDH or NADPH (Fig. 11B and C), indicating that endogenous cofactor levels could partially support BVMO catalysis under a high loading of the crude enzyme. The optimal GDH concentration was determined to be 75 μM, with higher concentrations resulting in diminishing returns (Fig. 11B and C). In summary, the introduction of a cofactor recycling system significantly enhances the catalytic efficiency of BVMO while allowing for reduced enzyme loading.

3.7. Reaction scale-up of the optimized system

To evaluate the industrial applicability of the multi-enzyme cascade, we scaled up the one-pot reaction under optimized conditions. Using 1 g of (5*E*,9*E*)-farnesyl acetone as the substrate, the entire reaction system was proportionally scaled, and product purification was achieved through recrystallization by exploiting the differential solubility of (−)-ambrox. In the first stage of the cascade, 200 mg wet cell weight of BVMO and esterase were added to the reaction mixture by crude enzymes, along with 1% Tween 80, 10 mM glucose, 30 μM FAD, 60 nM GDH and 10 μM NADPH. The reaction proceeded at 25 °C and 220 rpm for 12 hours. Without purification or buffer exchange, 400 mg wet cell weight of SHC and 0.06% SDS were then added directly to the same vessel, allowing the reaction to proceed at 37 °C and 220 rpm for an additional 12 hours. Following extraction with ethyl acetate, the crude product was concentrated, air-dried, and subsequently recrystallized. The resulting solid was dried in a vacuum oven to a constant weight. GC analysis of the purified material revealed a product purity of 98.8% and specific rotation $[\alpha] = -31°$, with only trace amounts of intermediate species (Fig. 12). High-purity (−)-ambrox with an 89.9% yield was obtained from 1 g of (5*E*,9*E*)-farnesyl acetone. These results demonstrate the feasibility and robustness of the one-pot cascade system for the selective, sustainable, and scalable production of high-value fragrance compounds.

4. Discussion

H. roseonigra has attracted attention for its unique ability to convert (−)-sclareol into (−)-sclareol glycol, a key intermediate that can undergo facile cyclization to (−)-ambrox. However, the development and application of this strain have been hampered by a lack of knowledge regarding its biosynthetic pathway. In this study, we employed transcriptomic analysis to identify a set of co-regulated enzymes and successfully reconstituted the pathway *in vitro* using chemically synthesized sclareol ketone as the substrate, leading to the enzymatic production of sclareol glycol. To the best of our knowledge, this represents the identification of the enzymes responsible for the conversion of sclareol acetone (compound **4**) to sclareol glycol. Transcriptomic data revealed that KEGG terms associ-

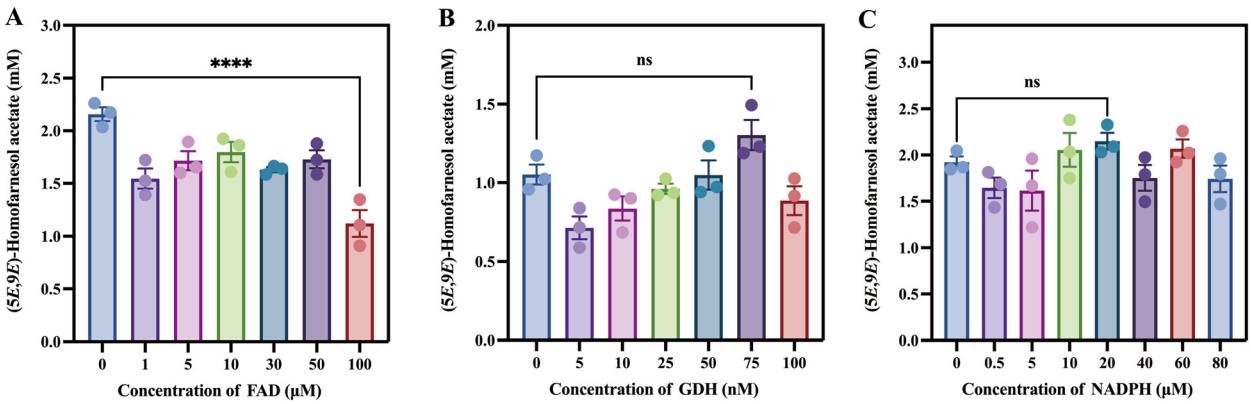

Fig. 11 The impact of cofactor recycling on BVMO catalytic activity under high enzyme loading (400 mg cell wet weight). (A) Effect of FAD on enzyme activity. (B) Effect of GDH on enzyme activity. (C) Effect of NADPH on enzyme activity.

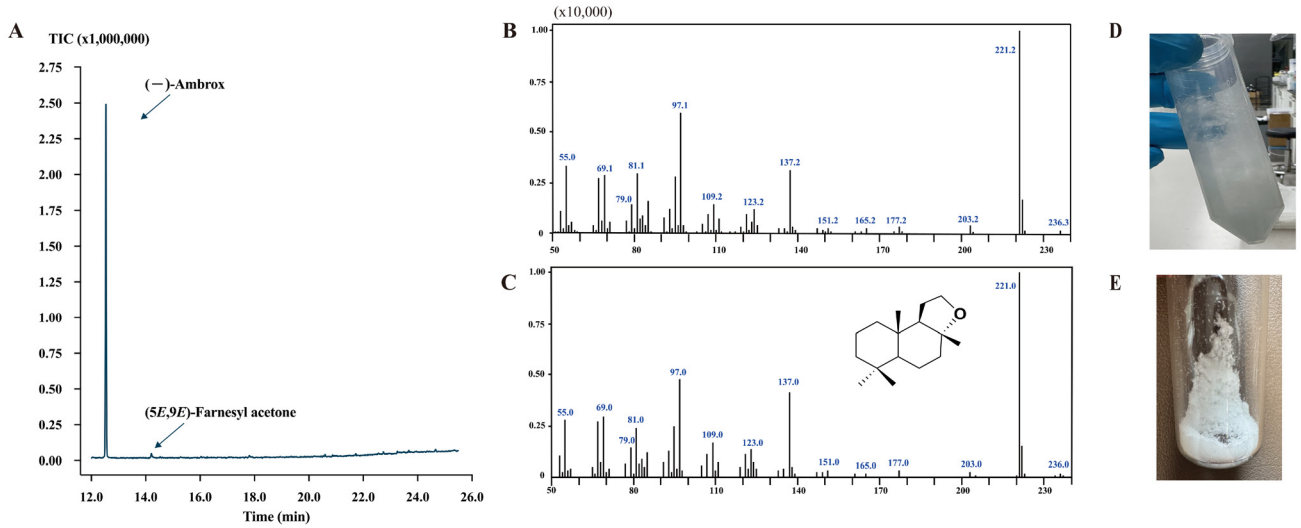

Fig. 12 Reaction scale-up of the optimized system. (A) Exemplary GC-MS total ion chromatograms of (−)-ambrox obtained by recrystallization after the scale-up reaction. A major peak of (−)-ambrox is observed with a minimal residual substrate ((5*E*,9*E*)-farnesyl acetone). (B) The mass spectrum of (−)-ambrox obtained by recrystallization after the scale-up reaction. (C) The mass spectrum of (−)-ambrox from the NIST library. (D) The physical state of (−)-ambrox after recrystallization and centrifugation. (E) (−)-Ambrox powder obtained by oven drying of the recrystallized precipitate.

ated with metabolic pathways and degradation of plant secondary metabolites were enriched, with concomitant downregulation of ribosomal components indicative of a classic stress-adaptation response that reallocates cellular resources from growth to defence and substrate processing.[38,39] The coordinated upregulation of BVMO, esterase, and associated catabolic enzymes during sclareol metabolism, combined with biochemical validation, strongly suggests their roles as the core drivers of a modular catabolic pathway, exemplifying a naturally evolved enzymatic strategy for the controlled degradation of terpenoid compounds.

Inspired by the biosynthetic pathway of (−)-sclareol glycol in *H. roseonigra*, we proposed a novel biocatalytic cascade for the synthesis of (−)-ambrox. This approach not only eliminates the use of toxic reagents but also has the potential to produce optically pure products owing to the inherent stereospecificity of the enzymes.[40,41–43] Given that *H. roseonigra* can utilize (−)-sclareol as its sole carbon source, it is reasonable to infer the presence of highly active BVMOs, esterases, and associated cofactor-regeneration enzymes.[19] This rationale underpinned our transcriptome-guided enzyme discovery strategy in *H. roseonigra*, which ultimately led to the identification of a co-regulated BVMO–esterase pair ideally suited for cascade catalysis. Interestingly, BVMO 2 was also shown to catalyse Baeyer–Villiger-type oxidation of an array of labdane aldehyde/ketone compounds, as shown in a patent disclosed by Givaudan.[44] However, neither the application of BVMO 2 on non-labdane-like substrates nor the co-expressed esterases has been reported, which allows efficient biocatalytic synthesis of (3*E*,7*E*)-homofarnesol, the key linear precursor for (−)-ambrox.[45]

Our computational findings corroborate observations from other studies that used MD simulations to link SHC dynamics with reactivity. For example, Schneider *et al*. performed *in silico* analysis to understand how remote mutations in *Tel*SHC (Y618L and G609F) led to improved catalysis.[32] Their simulations revealed that these mutations enlarged the active-site cavity and reduced the need for conformational rearrangements before cyclization, effectively pre-organizing the substrate in a reactive pose. Importantly, the catalytic DXDD motif remained intact in all the variants, confirming that the enhanced activity stemmed from physical tunnel reorganization rather than alterations in the active site chemistry.[46] These findings are consistent with emerging principles in SHC engineering, wherein expanding a cyclase's narrow tunnels and alleviating gating can dramatically increase catalytic efficiency.

As reported, the catalytic turnover (k_{cat}) of BVMOs is often limited not by the chemical transformation itself but by non-chemical steps such as conformational reorganization.[47] Large and hydrophobic substrates such as (5*E*,9*E*)-farnesyl acetone require significant conformational adaptation to fit into the BVMO active site.[48] In addition, the high hydrophobicity ($\log P \approx 5$) of (5*E*,9*E*)-farnesyl acetone likely reduces the binding affinity and structural stability, resulting in an observed K_M of 167.7 μM, which is comparable to that of several natural BVMOs that act on similar complex ketones.[49] The observed kinetic parameters indicate that this BVMO maintains favourable activity, even towards the energetically challenging substrate (5*E*,9*E*)-farnesyl acetone, making it particularly suitable for synthetic applications in the selective oxidative transformation of terpenoid scaffolds.

Considering that BVMO-catalysed reactions require essential cofactors, we hypothesized that the need for high cell density might stem from insufficient intracellular cofactor availability. Therefore, we sought to address this limitation by

introducing a cofactor recycling system to reduce overall cell loading. Although ADH was not functionally expressed in *E. coli*, we successfully reduced cell loading by introducing GDH for cofactor recycling. This highlights a well-known challenge in the heterologous expression of fungal enzymes in bacterial systems, where differences in the intracellular folding environment can severely limit functional expression.[50] These findings underscore the need for either host-specific expression systems or alternative enzyme mining strategies when reconstructing cofactor regeneration modules across distant phylogenetic boundaries. In summary, the introduction of a cofactor recycling system significantly enhanced the catalytic efficiency of BVMO while allowing for reduced enzyme loading. Moreover, the importance of NADPH recycling could be more pronounced at larger scales, particularly under the oxygen-rich conditions typical of aerobic bioprocesses.[50]

5. Conclusions

In this study, we successfully established a fully enzymatic, one-pot cascade for the sustainable synthesis of (−)-ambrox from *trans*-nerolidol, which can be produced at 26.4 g L^{-1} in *S. cerevisiae*. By integrating a BVMO, an esterase, and a semi-rationally engineered squalene–hopene cyclase, the cascade efficiently delivered the target fragrance molecule with excellent stereochemistry and 98.8% product purity. The reaction proceeded under mild, aqueous conditions with optimization of cofactors, thereby eliminating the need for hazardous oxidants or stoichiometric chemical reagents. Crucially, this approach bypasses the use of plant-derived feedstocks and organic solvents instead of leveraging benign enzymes and renewable intermediates. Through high selectivity, atom efficiency, and solvent minimization, this platform exemplifies multiple core tenets of green chemistry—including catalysis, safer reaction media, waste prevention, and energy efficiency. The developed cascade not only provides a greener and scalable alternative to traditional (−)-ambrox manufacturing but also achieves process-level simplicity through direct crystallization-based purification. Moreover, the success of this modular system—enabled by co-regulated enzyme discovery, SHC engineering, and cascade compatibility—underscores its potential adaptability to other high-value terpenoids or fine chemicals. The development of a modular chemo-enzymatic cascade for (−)-ambrox production represents more than an optimized route to produce a single fragrance compound—it establishes a potentially generalizable platform for converting linear terpenoid precursors into structurally complex products with non-canonical carbon skeletons. This approach addresses a fundamental limitation in traditional terpene biosynthesis, where the inherent carbon-count constraints of isoprene units (C_5) and their immediate oligomers (C_{10}, C_{15}, *etc.*) restrict structural diversity. Our methodology overcomes this limitation through the strategic integration of three key transformations: selective oxidative cleavage, chain modification, and stereocontrolled cyclization. Overall, this work provides a sustainable and industrially relevant strategy for (−)-ambrox production while laying a broader foundation for future applications of multi-enzyme cascades in green chemical manufacturing.

Author contributions

Jianjun Qiao, Qinggele Caiyin, Weiguo Li and Yi Zhang conceived the idea, directed the work and drafted the manuscript. Yi Zhang and Jianlin Liu designed the experiments, guided the data analysis, and wrote the manuscript draft. Jianlin Liu performed the transcriptional analysis, substrate scope, kinetics and optimization investigations, and scale-up reaction. Shaoping Zhang performed the semi-rational engineering of SHC. Weiguo Li and Jianlin Liu constructed a high-yield *trans*-nerolidol microbial cell factory. Jianlin Liu and Changle Zhao performed the instrument detection. Shengbin Zhou and Ganlu Zhang performed the chemical synthesis of compound **4**. Jianlin Liu and Xiaoguang Yan performed the kinetics analysis of BVMO and product purification. All authors reviewed the manuscript.

Conflicts of interest

The authors declare no conflicts of interest.

Data availability

All data supporting the conclusions of this study are included in the article/supplementary information (SI). Supplementary information is available. See DOI: https://doi.org/10.1039/d5gc05456g.

Further inquiries can be directed to the corresponding author Jianjun Qiao.

Acknowledgements

This work was financially supported by the National Key Research and Development Program of China (2020YFA0907900) and the Natural Science Foundation of Zhejiang Province (LQN25C010006).

References

1 M. Kanlayavattanakul, D. Mersni and N. Lourith, *Bot. Stud.*, 2024, **65**, 32.
2 C. Zhang and K. Hong, *Front. Bioeng. Biotechnol.*, 2020, **8**, 347.
3 E. Eichhorn and F. Schroeder, *J. Agric. Food Chem.*, 2023, **71**, 5042–5052.
4 C. Zhou, K. Peng, Y. Liu, R. Zhang, X. Zheng, B. Yue, C. Du and Y. Wu, *Animals*, 2023, **13**, 361.

5 A. Caniard, P. Zerbe, S. Legrand, A. Cohade, N. Valot, J.-L. Magnard, J. Bohlmann and L. Legendre, *BMC Plant Biol.*, 2012, **12**, 119.
6 J. Zhou, X. Xie, H. Tang, C. Peng and F. Peng, *Front. Pharmacol.*, 2022, 3–2022.
7 S. Wang, H. Yu, A. Yaras, B. Enkhchimeg, B. Gao and L. Mao, *Sci. Total Environ.*, 2024, **956**, 177156.
8 J. Xu, L. Liang, H. Zheng, Y. R. Chi and R. Tong, *Nat. Commun.*, 2019, **10**, 4754.
9 M. Schalk, L. Pastore, M. Mirata, S. Khim, M. Schouwey, F. Deguerry, V. Pineda, L. Rocci and L. Daviet, *J. Am. Chem. Soc.*, 2012, **134**, 18900–18903.
10 E. Eichhorn, B. Schilling, A. Bombrun and F. Schroeder, *Chimia*, 2024, **78**, 468–475.
11 L. A. Peterson, I. V. Ignatovich, A. E. Grill, A. Beauchamp, Y. Y. Ho, A. S. DiLernia and L. Zhang, *Chem. Res. Toxicol.*, 2019, **32**, 2214–2226.
12 N. Luo, M. Turberg, M. Leutzsch, B. Mitschke, S. Brunen, V. N. Wakchaure, N. Nöthling, M. Schelwies, R. Pelzer and B. List, *Nature*, 2024, **632**, 795–801.
13 E. N. Ncube, P. A. Steenkamp, C. W. van der Westhuyzen, L. H. Steenkamp and I. A. Dubery, *Catalysts*, 2022, **12**, 55.
14 M. D. Kerim, L. Evanno and L. Ferrié, *Chem. – Eur. J.*, 2023, **29**, e202203004.
15 L. Ruzicka, C. F. Seidel and L. L. Engel, *Helv. Chim. Acta*, 1942, **25**, 621–630.
16 S. Huang, S. L. Hong and X. Y. Zhao, *CN Pat*, 103755538B, 2015.
17 Y. Fang, Z. Wang, Y. Shi, F. Liu, J. Wang, T. Yang, Y. Xin, Z. Gu and L. Zhang, *Appl. Biochem. Biotechnol.*, 2023, **195**, 1184–1196.
18 E. N. Ncube, L. Sitole, P. A. Steenkamp, L. H. Steenkamp and I. A. Dubery, *Catalysts*, 2022, **12**, 1225.
19 M. Diao, C. Li, J. Li, J. Lu and N. Xie, *J. Agric. Food Chem.*, 2022, **70**, 10563–10570.
20 M. Šimek, S. Mahato, B. W. Dehnert and O. Kwon, *J. Am. Chem. Soc.*, 2025, **147**, 2664–2674.
21 D. Cao, M. Ataya, Z. Chen, H. Zeng, Y. Peng, R. Z. Khaliullin and C. J. Li, *Nat. Commun.*, 2022, **13**, 1805.
22 T. Morioka, A. Nishizawa, T. Furukawa, M. Tobisu and N. Chatani, *J. Am. Chem. Soc.*, 2017, **139**, 1416–1419.
23 D. H. Tran, K. Satou and T. B. Ho, *BMC Bioinf.*, 2008, **9**(Suppl 12), S5.
24 F. Hollmann, I. W. C. E. Arends and D. Holtmann, *Green Chem.*, 2011, **13**, 2285–2314.
25 S. Y. Li, K. Liu, Y. X. Chen, J. W. Guo and Z. Y. Zhao, *CN Pat*, 114921428A, 2022.
26 A. Bar-Even, E. Noor, Y. Savir, W. Liebermeister, D. Davidi, D. S. Tawfik and R. Milo, *Biochemistry*, 2011, **50**, 4402–4410.
27 D. Sheng, D. P. Ballou and V. Massey, *Biochemistry*, 2001, **40**, 11156–11167.
28 A. Hernández-Ortega, F. Lucas, P. Ferreira, M. Medina, V. Guallar and A. T. Martínez, *Biochemistry*, 2012, **51**, 6595–6608.
29 K. Hiraka, W. Tsugawa and K. Sode, *Int. J. Mol. Sci.*, 2020, **21**, 3797.
30 K. Kopylov, E. Kirilin and V. Švedas, *Biochem. Biophys. Res. Commun.*, 2023, **639**, 77–83.
31 W. Li, X. Yan, Y. Zhang, D. Liang, Q. Caiyin and J. Qiao, *J. Agric. Food Chem.*, 2021, **69**, 2236–2244.
32 A. Schneider, C. Curado, T. B. Lystbaek, S. Osuna and B. Hauer, *Angew. Chem., Int. Ed.*, 2023, **62**, e202301607.
33 E. Eric and U. Christophe, *WO Pat*, 2021110848A1, 2021.
34 K. S. Mthethwa, K. Kassier, J. Engel, S. Kara, M. S. Smit and D. J. Opperman, *Enzyme Microb. Technol.*, 2017, **106**, 11–17.
35 F. A. Sorgenfrei, J. J. Sloan, F. Weissensteiner, M. Zechner, N. A. Mehner, T. L. Ellinghaus, D. Schachtschabel, S. Seemayer and W. Kroutil, *Nat. Commun.*, 2024, **15**, 5420.
36 D. Niu, N. Zhao, J. Wang, N. P. McHunu, K. Permaul, S. Singh and Z. Wang, *Foods*, 2024, **13**, 2997.
37 M. Tomàs-Gamisans, C. C. P. Andrade, F. Maresca, S. Monforte, P. Ferrer and J. Albiol, *Appl. Environ. Microbiol.*, 2020, **86**, e02038-19.
38 Z. Cheng, C. F. Mugler, A. Keskin, S. Hodapp, L. Y. Chan, K. Weis, P. Mertins, A. Regev, M. Jovanovic and G. A. Brar, *Mol. Cell*, 2019, **73**, 36–47.
39 A. J. Larkin and K. Ragunathan, *FASEB J.*, 2022, **36**, L7761.
40 R. A. Sheldon and J. M. Woodley, *Chem. Rev.*, 2018, **118**, 801–838.
41 H. L. van Beek, R. T. Winter, G. R. Eastham and M. W. Fraaije, *Chem. Commun.*, 2014, **50**, 13034–13036.
42 E. Schütznerová and V. Krchňák, *J. Org. Chem.*, 2016, **81**, 3585–3596.
43 T. Sakoleva, F. Vesenmaier, L. Koch, J. E. Schunke, K. D. Novak, S. Grobe, M. Dörr, U. T. Bornscheuer and T. Bayer, *ChemBioChem*, 2025, **26**, e202400712.
44 S. Michel, D. Fabienne and S. E. Daniel, *US Pat*, 20230183761A1, 2023.
45 E. Eric and G. Andreas, *WO Pat*, 2022003017A1, 2022.
46 T. Xie, L. Zhou, L. Han, Z. Liu, W. Cui, Z. Cheng, J. Guo, Y. Shen and Z. Zhou, *Int. J. Biol. Macromol.*, 2024, **276**, 133642.
47 J. K. Crowell, S. Sardar, M. S. Hossain, F. W. Foss Jr. and B. S. Pierce, *Arch. Biochem. Biophys.*, 2016, **604**, 86–94.
48 P. Kokkonen, D. Bednar, V. Dockalova, Z. Prokop and J. Damborsky, *J. Biol. Chem.*, 2018, **293**, 11505–11512.
49 F. Desantis, M. Miotto, L. Di Rienzo, E. Milanetti and G. Ruocco, *Sci. Rep.*, 2022, **12**, 12087.
50 D. Chaulagain, N. S. Shamabadi, S. A. Leslie and D. K. Karig, *ACS Synth. Biol.*, 2024, **13**, 1165–1176.

